

2. EXPLANATORY NOTES¹

Shipboard Scientific Party²

INTRODUCTION

This chapter explains the techniques and procedures used during Leg 188 in order to help document the basis for our preliminary scientific conclusions and to provide the interested investigator with the information needed to select samples for further analysis. This information concerns only shipboard operations and analyses described in the site reports in the Leg 188 *Initial Reports* volume of the *Proceedings of the Ocean Drilling Program*. Methods used by various investigators for shore-based analyses of Leg 188 data will be described in the individual scientific contributions published in the *Scientific Results* volume and in publications in various professional journals.

Authorship of Site Chapters

The separate sections of the site chapters were written by the following shipboard scientists (authors are listed in alphabetical order; no seniority is implied):

Principal Results: Cooper, O'Brien
Background and Objectives: Cooper, O'Brien
Operations: Richter, Storms
Site Geophysics: Cooper, O'Brien
Lithostratigraphy: Damuth, Januszczak, Kaiko, Passchier, Rebesco, Strand, Theissen, Warnke
Biostratigraphy: Bohaty, Pospichal, Quilty, Whalen, Whitehead
Paleomagnetism: Erwin, Florindo, Richter
Inorganic Geochemistry: Kryc, Lavelle
Organic Geochemistry: Claypool
Physical Properties: Forsberg, Grützner, Taylor
In Situ Temperatures: Kaiko

¹Examples of how to reference the whole or part of this volume.

²Shipboard Scientific Party addresses.

Downhole Measurements: Barr, Handwerger, Williams

Use of “Ma” vs. “m.y.”

1. The term *Ma* is equivalent to and replaces m.y.B.P. (million years before present); for example, 35–40 Ma.
2. The term *m.y.* is used in the context of duration, such as “... for 5 m.y. in the early Miocene.”

Drilling Characteristics

Information concerning sedimentary stratification in uncored or unrecovered intervals may be inferred from seismic data, wireline-logging results, and examination of the behavior of the drill string, as observed and recorded on the drilling platform. Typically, the harder a layer, the slower and more difficult it is to penetrate. A number of other factors may determine the rate of penetration, so it is not always possible to relate the drilling time directly to the hardness of the layers. Bit weight and revolutions per minute (rpm), recorded with a new acquisition program (Fusion), also influence the penetration rate.

Drilling Deformation

When cores are split, many of them show signs of significant drilling disturbance, including the concave-downward appearance of originally horizontal bedding, haphazard mixing of lumps of different lithologies (mainly at the tops of cores), fluidization, and flow-in. Core deformation may also occur during retrieval because of changes in pressure and temperature as the core is raised, as well as during cutting and core handling on deck.

Shipboard Scientific Procedures

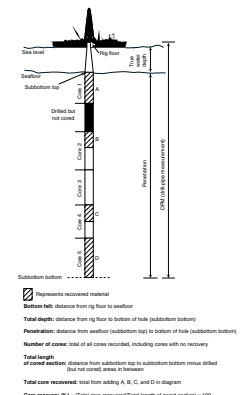
Numbering of Sites, Holes, Cores, and Samples

Ocean Drilling Program (ODP) drill sites are numbered consecutively and refer to one or more holes drilled while the ship was positioned over one acoustic beacon. Multiple holes may be drilled at a single site by pulling the drill pipe above the seafloor (out of the hole), moving the ship some distance from the previous hole, and then drilling another hole.

For all ODP drill sites, a letter suffix distinguishes each hole drilled at the same site. The first hole drilled is assigned the site number modified by the suffix “A,” the second hole takes the site number and suffix “B,” and so forth. Note that this procedure differs slightly from that previously used by the Deep Sea Drilling Project (DSDP) (Sites 1 through 624) but prevents ambiguity between site- and hole-number designations. It is important to distinguish among holes drilled at a site because recovered sediments or rocks from different holes usually do not come from exactly equivalent positions in the stratigraphic column.

The cored interval is measured in meters below seafloor (mbsf). The depth interval assigned to an individual core begins with the depth below the seafloor at which the coring operation began and extends to the depth at which the coring operation ended (Fig. F1). Each cored interval is generally 9.5 m long, which is the length of a core barrel. Coring intervals may be shorter and may not necessarily be continuous if

F1. Coring and depth intervals, p. 40.



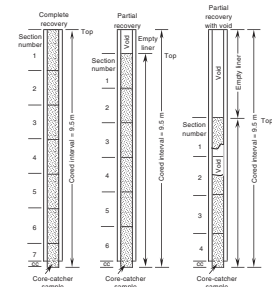
separated by drilled intervals. In soft sediments, the drill string can be “washed ahead” with the core barrel in place, without recovering sediments. This is achieved by pumping water down the pipe at high pressure to wash the sediment out of the way of the bit and up the space between the drill pipe and the wall of the hole.

Cores taken from a hole are numbered serially from the top of the hole downward. Core numbers and their associated cored intervals (in mbsf) ideally are unique in a given hole; however, this may not be true if an interval is cored twice, if the borehole wall caves in, or if other hole problems occur. The full recovery length for a single core is 9.5 m of rock or sediment contained in a plastic liner (6.6 cm internal diameter) plus ~0.2 m (without a plastic liner) in the core catcher (Fig. F2). The core catcher is a device at the bottom of the core barrel that prevents the core from sliding out when the barrel is being retrieved from the hole. In many advanced hydraulic piston corer/extended core barrel (APC/XCB) cores, recovery exceeds the 9.5-m theoretical maximum by as much as 0.60 m. The cause of this expansion is not fully understood. The recovered core in its liner is divided into 1.5-m sections that are numbered serially from the top (Fig. F2). When full recovery is obtained, the sections are numbered from 1 through 7, with the last section generally being shorter than 1.5 m. Rarely, a core may require more than seven sections; this is usually the result of voids within some sections caused by gas expansion. When less than full recovery is obtained, as many sections as are needed to accommodate the length of the core will be recovered; for example, 4 m of core would be divided into two 1.5-m sections and a 1-m section. If cores are fragmented (recovery <100%), sections are numbered serially and intervening sections are noted as void, whether or not shipboard scientists believe that the fragments were contiguous. In rare cases, a section <1.5 m may be cut to preserve features of interest. Sections <1.5 m in length are also sometimes cut when the core liner is severely damaged.

By convention, material recovered from the core catcher is placed immediately below the last section when the core is described and is labeled core catcher (CC); in sedimentary cores, it is treated as a separate section. In cases where material is recovered only in the core catcher, it is assigned the depth of the top of the cored interval (this convention differs from that used in the early days of DSDP), although information from the driller or other sources may indicate from what depth it was actually recovered.

When the recovered core is shorter than the cored interval, the top of the core is equated with the top of the cored interval by convention to achieve consistency when handling analytical data derived from the cores. Samples removed from the cores are designated by distance, measured in centimeters from the top of the section to the top and bottom of each sample removed from that section. A complete identification number for a sample consists of the following information: leg, site, hole, core number, core type, section number, piece number (for hard rock), and interval in centimeters, measured from the top of the section. For example, a sample identification of “188-1165A-11H-6, 10–12 cm,” would be interpreted as representing a sample removed from the interval between 10 and 12 cm below the top of Section 6, Core 11 (H designates that this core was taken by the APC) of Hole 1165A during Leg 188. A computer routine is available to calculate the mbsf depth from any correctly formulated ODP sample designation. This avoids any inconsistencies caused by cutting some sections to nonstandard lengths.

F2. Examples of numbered core sections, p. 41.



All ODP core and sample identifiers indicate core type. The following abbreviations are used: H = hydraulic piston core (HPC; also referred to as APC), X = XCB, and R = rotary core barrel (RCB). APC, XCB, and RCB cores were cut during Leg 188.

Core Handling

As soon as a core was retrieved on deck, a sample taken from the core catcher was given to the paleontological laboratory for an initial age assessment. Special care was taken in transferring the core from the drill floor to a long horizontal rack on a catwalk near the core laboratory so that the core did not bend or twist excessively. The core was capped immediately, and gas samples were taken by piercing the core liner and withdrawing gas into a vacuum tube. Voids within the core were sought as sites for gas sampling. Some of the gas samples were stored for shore-based study, but others were analyzed immediately as part of the shipboard safety and pollution-prevention program. Next, the core was marked into section lengths of 150 cm, each section was labeled, and the core was cut into sections. Interstitial water (IW) and whole-round samples were also taken at this time. In addition, headspace gas samples were taken from the end of cut sections on the catwalk and sealed in glass vials for light hydrocarbon analysis. Afterward, each section was sealed at the top and bottom by gluing on color-coded plastic caps: blue to identify the top of a section and clear for the bottom. A yellow cap was placed on the section ends from which a whole-round sample was removed. The caps were usually attached to the liner by coating the end liner and the inside rim of the cap with acetone.

The cores were then carried into the laboratory, where the sections were labeled with an engraver to permanently mark the complete designation of the section. The length of the core in each section and the core-catcher sample were measured to the nearest centimeter. This information was logged into the shipboard Oracle database (Janus).

After equilibrating to room temperature for ~3–4 hr, whole-round sections from APC and XCB cores were routinely run through the multisensor track (MST). The MST includes a gamma-ray attenuation (GRA) bulk densiometer, a *P*-wave logger, natural gamma-ray emission measurement, and a volume magnetic susceptibility meter. Soft sediments were measured for thermal conductivity before being split lengthwise into working and archive halves. Softer cores were split with a wire; harder cores were split using a diamond saw. The wire-cut cores were split from top to bottom so that sediment below the empty space or soupy intervals (as are sometimes present at the top of Section 1) would not be drawn into the empty space or compress the soupy materials at the top of a section.

After splitting, the halves of the core were designated as working and archive halves, respectively. Archive halves were then described visually and run through the ODP Minolta color scanner and the cryogenic magnetometer. Finally, the cores were photographed with both black-and-white and color film, a whole core at a time. Close-up photographs (black-and-white and color) were taken of particular features, as requested by individual scientists, for illustrations in the summary of each site.

The working half of the core was measured first for sonic velocity. After physical properties and paleomagnetic sampling, the working half was sampled for shipboard and shore-based laboratory studies. Each sample taken either for shipboard or shore-based analysis was logged

into the Oracle database (Janus) by the location and name of the investigator receiving the sample. Records of all of the samples removed are kept in the Janus database and by the curator at ODP headquarters. The extracted samples were sealed in plastic bags and labeled.

Both halves of the core were placed into labeled plastic tubes, which were then sealed and transferred to cold-storage space aboard the drilling vessel. At the end of the leg, the cores were transferred from the ship in refrigerated air-freight containers to cold storage at the ODP core repository in Bremen/Germany.

LITHOSTRATIGRAPHY

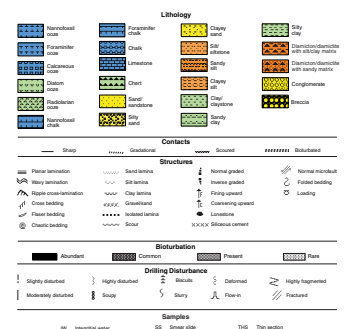
This section outlines the procedures followed to document the basic sedimentology of the deposits recovered during Leg 188, including core description, X-ray diffraction (XRD), X-radiography, color spectrophotometry, and smear-slide description. Only general procedures are outlined, except where they depart significantly from ODP conventions.

Visual Core Descriptions

Information from macroscopic description of each core was recorded manually for each core section on visual core-description (VCD) forms. A wide variety of features that characterize the sediment were recorded, including lithology, sedimentary structures, color, and sediment deformation. Compositional data were obtained from smear slides. The color (hue and chroma) of the sediments was determined visually using the Munsell soil color charts (1975). This information was condensed and entered into AppleCORE (version 8.1b) software, which generates a simplified, one-page graphical description of each core (barrel sheet). Barrel sheets are presented with split-core photographs (see the “[Core Descriptions](#)” contents list). The lithologies of the recovered sediments are represented on barrel sheets by symbols in the column entitled “Graphic Lithology” (Fig. F3).

Primary sedimentary structures, bioturbation parameters, soft-sediment deformation, structural features, and drilling disturbance are indicated in columns to the right of the graphic log. The symbols are schematic but are placed as close as possible to their proper stratigraphic position. For exact positions of sedimentary features, the more detailed VCDs can be obtained from ODP. Deformation and disturbance of sediment that resulted from the coring process are illustrated in the “Drilling Disturbance” column. Blank regions indicate the absence of coring disturbance. Locations of samples taken for shipboard analysis are indicated in the “Samples” column. A summary lithologic description with sedimentologic highlights is given in the “Description” column of the barrel sheet. This description provides information about the major sediment lithologies; important minor lithologies; and an extended summary description of the sediments, including color, composition, sedimentary structures, trace fossils identified and extent of bioturbation, and other notable characteristics. Descriptions and locations of thin, interbedded, or minor lithologies that could not be depicted in the “Graphic Lithology” column are also presented in “Description,” where space permits.

F3. Key to symbols used in Leg 188 barrel sheets, p. 42.



Sediment Classification

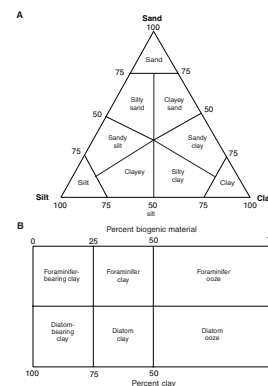
The sediment classification scheme used during Leg 188 is descriptive and follows the ODP classification (Mazullo et al., 1988), with some simplifying modifications for sediments that are mixtures of siliciclastic and biogenic components (Fig. F4) and an additional classification of gravel-rich sediments (Fig. F5). Classification is based primarily on macroscopic description of the cores and examination of smear slides. During Leg 188, the total calcium carbonate content of the sediments determined on board (see “Organic Geochemistry,” p. 20, and “Inorganic Geochemistry,” p. 19) was also used to aid in classification. Composition and texture are the criteria used to define lithology. Genetic terms such as pelagic, neritic, hemipelagic, and debris flow do not appear in this classification. The term *clay* is used only for particle size and is applied to both clay minerals and other siliciclastic material <4 μm in size.

The principal name applied to a sediment is determined by the component or group of components (e.g., total biogenic carbonate) that comprise(s) >50% of the sediment or rock, except for subequal mixtures of biogenic and siliciclastic material. If the total of a siliciclastic component is >50%, the main name is determined by the relative proportions of sand, silt, and clay sizes when plotted on a modified Shepard (1954) classification diagram (Fig. F4A). Examples of siliciclastic principal names are clay, silt, sand, silty clay, sandy clay, clayey silt, sandy silt, clayey sand, and silty sand. However, if the total of biogenic components is >50% (i.e., siliciclastic material <50%), then the principal name applied is *ooze* (Fig. F4B). Biogenic components are not described in textural terms. Thus, a sediment with 45% sand-sized foraminifers and 55% siliciclastic clay is called foraminifer clay, not foraminifer clayey sand.

In mixtures of biogenic and nonbiogenic material where the biogenic content is 25%–50% (termed *mixed sediments* in the ODP classification), the name consists of two parts: (1) a major modifier(s) consisting of the name(s) of the major fossil(s), with the least common fossil listed first, followed by (2) the principal name appropriate for the siliciclastic components (e.g., foraminifer clay) (Fig. F4B). If any component (biogenic or siliciclastic) represents <25% of a sediment, it qualifies for minor modifier status and is hyphenated with the suffix *-bearing* (e.g., nannofossil-bearing clay). In cases of approximately subequal mixtures of calcareous microfossils, the modifiers *calcareous* or *carbonate bearing* can be used instead of microfossil names (e.g., calcareous clay). Examples include 11% foraminifers, 34% nannofossils, and 55% clay = foraminifer-bearing nannofossil clay; 20% diatoms and 80% foraminifers = diatom-bearing foraminifer ooze.

The objectives of Leg 188 were to examine depositional processes and the history of climate change along the glacially influenced continental margin of Prydz Bay. In such settings, an important sediment type is represented by poorly sorted diamict facies. The term *diamict* is used here as a nongenetic term for materials consisting of matrix-supported admixtures of gravel-sized clasts. It should be noted that existing ODP classifications do not adequately address nonsorted or poorly sorted admixtures of siliciclastic sediments, such as diamicts. During Leg 119, poorly sorted admixtures of gravel and fine-grained sediment were covered by one term (diamictite) (Shipboard Scientific Party, 1989). During Leg 188, the classification of poorly sorted sediments containing gravel (Fig. F5) is based on Moncrieff (1989) to allow distinc-

F4. Classification scheme for siliciclastics and procedure for naming mixtures of biogenic and siliciclastic sediments, p. 43.



F5. Classification of poorly sorted sediments with a gravel component, p. 44.

		Percent gravel (>2 mm) in whole rock estimated from core			
		0-10%	10-20%	20-40%	>40%
Percent silt in matrix	0	CLAY/SILT with dispersed clasts	CLAY/SILT with common clasts	CLAY/SILT with abundant clasts	CLAY/SILT with abundant clasts
	50	* CLAY/SILT with dispersed clasts	CLAY/SILT with dispersed clasts	CLAY/SILT with dispersed clasts	CLAY/SILT with dispersed clasts
100	FINE-GRAINED SEDIMENTS	* SAND with dispersed silt	SAND with dispersed silt	SAND with dispersed silt	SAND with dispersed silt
		SAND with dispersed silt	SAND with common silt	SAND with abundant silt	SAND with abundant silt

tion of clast-poor and clast-rich facies with different sand contents. Matrix grain size in diamicts was described using the Shepard (1954) diagram in Figure F4A. To determine clast content, we adopted the comparison chart for visual percentage estimation as presented by Mazzullo et al. (1988; their fig. 16). A visual percentage estimate of 10% gravel clasts is taken as the boundary between clast-poor and clast-rich lithologies.

The term *clast* refers to both sand and gravel-sized components, *lone-stones* are gravel-sized (>2 mm) clasts, and *grains* are floating silt and sand in a fine matrix. *Granules* are 2–4 mm in size, and *pebbles* are >4-mm-large clasts (following the Wentworth scale [1922]). The term *lone-stone* is restricted to gravel-sized clasts in a fine-sediment matrix, whereas *pebbles* or *granules* can be present without matrix.

Induration

The following classes of induration or lithification were adopted and modified from ODP Leg 105 (Shipboard Scientific Party, 1987). They were separated into three classes for biogenic sediments and two classes for nonbiogenic sediments.

For biogenic sediments and sedimentary rocks, the three classes of induration are

1. Soft: ooze; has little strength and is readily deformed under pressure of a finger or broad blade spatula;
2. Firm: chalk, diatomite, radiolarite; partly lithified and readily scratched with a fingernail or the edge of a spatula; and
3. Hard: limestone, porcellanite, chert; well lithified and cemented, resistant or impossible to scratch with a fingernail or the edge of a spatula.

For nonbiogenic clastic sediments, the two classes of induration are

1. Soft: diamicton, gravel, sand, silt, clay; sediment core can be split with a wire cutter; and
2. Hard: diamictite, conglomerate, sandstone, siltstone, claystone; cannot be compressed with finger pressure, or core must be cut with a band saw or diamond saw. The term *diamict* is used for both soft and hard sediments and includes diamictons and diamictites.

X-Ray Diffraction

Relative abundances of the main silicate and carbonate minerals were determined semiquantitatively using a Philips APD 3720 X-ray diffractometer with CuK_α radiation (Ni filter), operated by Philips software PCAPD 3.0. Each bulk-sediment sample was freeze dried, crushed, and mounted with a random orientation into an aluminum sample holder. Instrument conditions were as follows: 40 kV, 35 mA, goniometer scan from 2° to $70^\circ 2\theta$ for bulk samples, step size = $0.01^\circ 2\theta$, scan speed at $1.2^\circ 2\theta/\text{min}$, count time = 0.5 s. Peak intensities were converted to values appropriate for a fixed slit width. An interactive software package (MacDiff 4.0.4 PPC) was used on a Macintosh computer to identify the main minerals. Diffractograms were peak corrected to match the main quartz peak at 3.343 \AA . In the absence of quartz, no peak correction was applied. Identifications were based on multiple peak matches using the

mineral database provided with MacDiff. Relative proportions of quartz, feldspar, clay minerals, and accessory minerals were plotted using the methods of Forsberg et al. (1999). Relative abundances reported in this volume are useful for general characterization of the sediments, but they are not precise quantitative data.

Clay mineralogy was examined by XRD on separate 3-g samples that were placed in a 50-mL centrifuge tube with 10% acetic acid, sonicated for 15 min, and allowed to stand overnight to remove carbonate material. After centrifuging for 15 min at 1500 rpm, the acetic acid was decanted, 25 mL of distilled water was added, the sample was centrifuged again, and the water was decanted. This washing was repeated two more times to remove salt from the sample. After decanting the final wash water, 25 mL of Calgon solution was added to the sample in a 50-mL beaker. The sample was then placed in a sonic dismembrator for as long as 90 s to suspend the clays by ultrasonic disaggregation then centrifuged for 5 min at 1000 rpm to settle the >2- μm particles. The clays that remained in suspension were removed from the top 1 cm of the centrifuge tube and collected by vacuum filtration on a 0.45- μm Millipore filter. The filter was removed and cut in half to prepare two identically oriented clay slides. The clay was transferred to the slide by placing the filter on the slide and rolling the back of the filter with a small roller. The slides used were high-resolution quartz mounts, cut normal to the C-axis for zero-background analysis. One slide was air dried and analyzed, then solvated with ethylene glycol for at least 12 hr and reanalyzed to determine the presence of expandable clays. The second slide was analyzed after being heated to 550°C for 1 hr to collapse kaolinite and smectite. All oriented clay mounts were scanned from 2° to 35°2 θ in 0.010° increments.

Smear Slides and Thin Sections

Petrographic analysis of the sand- and silt-sized components of the sediment was primarily by smear-slide description. Tables summarizing data from smear slides are available (see the “[Core Descriptions](#)” contents list). These tables include information about the sample location, whether the sample represents a dominant (D) or a minor (M) lithology in the core, and the estimated percentage ranges of sand, silt, and clay, together with all identified components. We emphasize here that smear-slide analysis provides only crude estimates of the relative abundances of detrital constituents. The mineral identification of finer grained particles can be difficult using only a petrographic microscope, and sand-sized grains tend to be underestimated because they cannot be evenly incorporated into the smear. The mineralogy of smear-slide components was validated by XRD. The relative proportions of carbonate and noncarbonate materials estimated from smear slides was validated by chemical analysis of the sediments (see “[Inorganic Geochemistry](#),” p. 19). Thin-section descriptions were used to verify the composition of gravel-sized clasts in diamicts and the composition of limestones. For selected clasts, the texture and lithologic composition are determined (see the “[Core Descriptions](#)” contents list).

Spectrophotometer

Reflectance of visible light from the surface of cores was routinely measured downcore using a Minolta spectrophotometer (model CM-2002) mounted on the archive multisensor track (AMST). The AMST

measures the archive half of each core section. The purpose of measuring the visible light spectra was to provide a continuous stratigraphic record of color variations downcore for visible wavelengths (VIS 400–700 nm). Spectrophotometer readings were taken after cleaning the surface of each core section. The measurements were then automatically taken and recorded by the AMST, which permits measurements only at evenly spaced intervals along each core. Each measurement consists of 31 separate determinations of reflectance in 10-nm-wide spectral bands from 400 to 700 nm. Additional detailed information about measurement and interpretation of spectral data with the Minolta spectrophotometer can be found in Balsam et al. (1997, 1998, 1999) and Balsam and Damuth (2000).

X-Radiography

X-radiography was conducted using a portable VR1020 X-ray unit with a highly focused columnator, designed for field use by veterinarians. Before the cruise, the unit was tested by ODP at Texas A&M University for radiation leakage and was found to have no primary leakage. The Texas A&M group established that the unit was safe for operation without radiation protection, substantiating the manufacturer's claim of safety for this standard operating method.

The X-ray unit was mounted semipermanently above a table covered by lead shielding directly inside the doorway from the core-catwalk into the sediment laboratory (Fig. F6). This location allowed quick transport of newly recovered cores to the X-ray table, if needed, for hydrate studies. X-ray images were made using 8 in × 10 in film packs (Kodak Industrex Ready-Pack II-AA film). Either one or two cores could be imaged simultaneously using the specially prepared wood holders on which cores were placed for the X-radiograph. The film was placed under the cores, with lead-letter identification labels. Measurements of the exact core intervals were made, and a photograph was taken using a digital camera for verification of placement of core and film.

The following exposures were most commonly used to give good X-ray images: for whole-round cores, 50 mA/100 kV (full power); for half-round cores, 50 mA/66 kV. The film was developed by an ODP staff photographer using the same general procedures for developing images from the ship's medical X-ray unit. Specifically, Kodak Tmax RS developer was used at 75°F for 4 min, followed by 30 min in a stop bath; then fixed for 4 min, with two washes at 20 and 10 min; and finally dried.

After the images were dried, they were placed on a light table and again photographed with a digital camera. The X-ray films and paper copies of the core and X-ray photos were submitted to ODP as part of the primary data from the cruise.

BIOSTRATIGRAPHY AND SEDIMENTATION RATES

Introduction

Results from ODP Legs 113, 114, 119, and 120 greatly improved southern high-latitude Cenozoic and Late Cretaceous biostratigraphy. The study of sediments recovered during these legs provided biostratigraphic zonations using both calcareous and siliceous microfossils with

F6. The X-ray unit in the entry area of the core laboratory, p. 45.



the additional resolution of stratigraphic ranges that could be tied directly to the geomagnetic time scale (e.g., Gersonde et al., 1990; Barron et al., 1991; Harwood et al., 1992). Leg 188 drilling in Prydz Bay allowed further testing and possible refinement of these biostratigraphic schemes and the intercalibration of high- and mid-latitude zonations and species ranges. Improved dating of Neogene biostratigraphic ranges may be accomplished by correlation with isotopic stratigraphies or other data sets with high temporal resolution, such as color reflectance, magnetic susceptibility, and magnetic paleointensity records. In addition, Prydz Bay drilling provided a unique opportunity for documenting and understanding evolutionary processes (patterns, modes, and timing of speciation and diversification), the development of Southern Hemisphere bioprovinces, and the response of the biota to long- and short-term environmental changes related to paleogeographic and cryospheric evolution in southern high latitudes.

Calcareous nannofossils, planktonic and benthic foraminifers, diatoms, and radiolarians were examined for Leg 188 biostratigraphic assessment. Preliminary ages were assigned primarily based upon core-catcher samples; however, selected samples from within the cores were examined for additional resolution. Ages for calcareous nannofossil, foraminiferal, diatom, and radiolarian events and epoch boundaries are based on the geomagnetic polarity time scale (GPTS) of Berggren et al. (1995b) and Cande and Kent (1995). Age models were based primarily on biostratigraphic datums as well as magnetostratigraphic chron and subchron boundaries correlated with the GPTS. For sedimentation rate calculations, it was necessary to employ additional high-latitude biostratigraphic datums (e.g., Wei, 1992; Harwood et al., 1992) not presented in Berggren et al. (1995b).

Calcareous Nannofossils

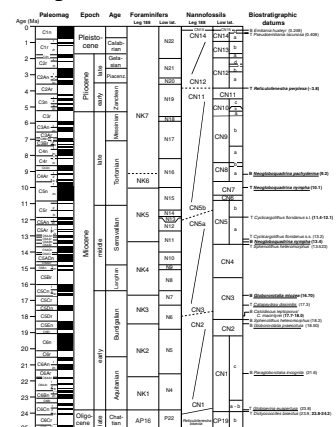
Biostratigraphy

The cosmopolitan nannofossil biostratigraphic schemes of Martini (1971) and Okada and Bukry (1980) were used with major modifications. The absence of low- to mid-latitude marker species in the Southern Ocean necessitated the combination of many of the zones, particularly in the Neogene (Pospichal et al., 1992) (Fig. F7). Wei and Wise (1992a, 1992b) calibrated several useful Neogene high-latitude nannofossil datums to the paleomagnetic time scale (subsequently recalibrated by Berggren et al., 1995b). About five useful zones were used for the austral high-latitude Neogene.

Higher resolution is possible for the Oligocene to mid-middle Eocene (Wise, 1983; Wei and Wise, 1990; Wei and Thierstein, 1991) (Fig. F7). Ages for key datum levels have been calibrated in the region of the Kerguelen Plateau against magnetostratigraphy by Wei and Wise (1992b); these are indicated in bold type on Figure F7, where they are shown against the Berggren et al. (1995b) time scale.

As noted by Wei and Wise (1992b), biomagnetostratigraphic correlations at several Southern Ocean sites may show considerably different ages relative to those compiled from the mid-latitudes by Berggren et al. (1985, 1995b). Where such differences exist, we have chosen to use ages derived from the high-latitude calibrations. Where such ages differ from those in the lower latitudes, the high-latitude ages are shown in bold type in Figure F7 following the corresponding datum level (similarly, high-latitude biostratigraphic datums are also indicated in bold type).

F7. Holocene through Paleogene time scale with foraminifer and nannofossil biostratigraphic datums, p. 46.



For major differences in age assignment, arrows indicate where on the chart a datum has been repositioned for the purposes of this leg.

Methods

Smear slides were prepared for calcareous nannofossil study using standard techniques. Slides were examined using a light microscope under crossed polarizers, transmitted light, and phase-contrast light at 1000× or 1200× magnification. Preservation and abundance of calcareous nannofossil species varied significantly due to etching, dissolution, or calcite overgrowth. Preservation was indicated as follows:

- VG= very good preservation (no evidence of dissolution and/or overgrowth; no alteration of primary morphological characteristics and specimens appear diaphanous; specimens were identifiable to the species level).
- G = good preservation (little or no evidence of dissolution and/or overgrowth; primary morphological characteristics are only slightly altered; specimens were identifiable to the species level).
- M = moderate preservation (specimens exhibit some etching and/or overgrowth; primary morphological characteristics are sometimes altered; however, most specimens were identifiable to the species level).
- P = poor preservation (specimens are severely etched or exhibit overgrowth; primary morphological characteristics are largely destroyed; fragmentation has occurred; most specimens could be identified to the species and/or generic level).

Six calcareous nannofossil abundance levels were recorded as follows:

- V = very abundant (>10 specimens per field of view).
- A = abundant (1–10 specimens per field of view).
- C = common (1 specimen per 2–10 fields of view).
- F = few (1 specimen per 11–100 fields of view).
- R = rare (1 specimen per 101–1000 fields of view).
- B = barren.

Planktonic and Benthic Foraminifers

Several planktonic foraminiferal zonal schemes have been developed for the mid- and high latitudes of the Southern Hemisphere (e.g., Jenkins and Srinivasan, 1986; Berggren, 1992a, 1992b); however, these schemes are not fully applicable to the planktonic foraminiferal fauna in all the sections recovered during Leg 188 because of the absence or low abundance of foraminiferal species, particularly in the Neogene. In general, high-latitude foraminiferal assemblages contain low-diversity and long-ranging species that are of limited biostratigraphic use. Planktonic foraminiferal zonation and classification followed Berggren (1992a, 1992b). Recent experience on Mac. Robertson Shelf (Quilty et al., 2000) and on the southern Kerguelen Plateau (Berggren, 1992a, 1992b) indicates that the diversity of planktonic foraminifers may have been greater during the Paleogene and that lower latitude zonal schemes may be applicable. Thus, the scheme of Berggren (1992a, 1992b) is illustrated in Figure F7. Future examination of the fine frac-

tions (63–125 μm) may also yield additional species (Li and Radford, 1992).

Although benthic foraminifers generally provided limited biostratigraphic age control, all zones recognized were local assemblage zones (e.g., Mackensen and Berggren, 1992), and they were useful in paleoenvironmental reconstruction.

At Site 1097 (Leg 178), three foraminiferal biofacies (Biofacies A, B, and C) aided the interpretation of late Neogene lithofacies (Shipboard Scientific Party, 1999c). This approach was applied to Leg 188 sediments to further characterize glacial marine sedimentary environments in Prydz Bay. Biofacies A consists of poorly preserved reworked assemblages of benthic foraminifers. Characteristic samples contain <12 robust foraminifer specimens (typically the benthic foraminifers *Globocassidulina subglobosa* and *Cassidulinoides parkerianus*), which are commonly yellow colored, broken, or filled with sediment, indicating postmortem transport.

Biofacies B yields moderately preserved, more abundant and diverse assemblages in which *G. subglobosa* and *C. parkerianus* are again dominant, but preservation is better than in Biofacies A.

Biofacies C consists of large numbers (as many as 1000 specimens) of well-preserved foraminifers in association with other well-preserved biogenic material.

Biofacies A is characteristic of massive diamictite lithofacies, Biofacies B is typical of stratified and graded diamictites interbedded with bioturbated mudstones, and Biofacies C occurs in massive diamictites that are transitional to bioturbated muddy sands with ice-rafted clasts.

Methods

Core-catcher samples of $\sim 20\text{ cm}^3$ were soaked in tap water, disaggregated, wet sieved over a 63- μm sieve, and dried in an oven at temperatures $\leq 60^\circ\text{C}$. Several different methods were used for disaggregation, including ultrasonic treatment, heating on a hot plate, or using Calgon solution and hydrogen peroxide for consolidated sediments. Well-indurated samples were subjected to repeated drying and wetting to break up the sample. Between successive samples, the sieves were soaked in water containing methylene blue in order to stain specimens left in the sieves from previous samples. Foraminifers were separated and identified under a stereobinocular microscope. The abundance of planktonic foraminifers relative to the total sieved residue was categorized as follows:

- A = abundant (<50% of the total sieved residue).
- C = common (>25%–50% of the total sieved residue).
- F = few (5%–25% of the total sieved residue).
- R = rare (<5% of the residue).
- B = barren (no specimens in sample).

Benthic foraminifer species abundances were recorded as follows:

- D = dominant (>50% of total assemblage).
- A = abundant (>10%–50% of total assemblage).
- C = common (>1%–10% of total assemblage).
- F = few (0.1%–1.0% of total assemblage).
- R = rare (<0.1% of total assemblage).

B = barren (no specimens observed).

Foraminifer preservation was categorized as follows:

G = good (dissolution effects were rare).

M = moderate (dissolution damage such as etched and partially broken tests or fragments occurred frequently).

P = poor (the degree of fragmentation was often high, and the specimens present were small, encrusted, and possibly reworked).

Bolboforma

Bolboforms are an extinct group of calcareous plankton that lived in temperate to cold conditions; they have characterized sub-Antarctic water masses and may provide useful biostratigraphy in southern high-latitude sites. They are placed in the family Bolboformaceae of the class Chrysophyceae (Tappan, 1980). Thirteen zones have been established for the Eocene to upper Pliocene (Spiegler and von Daniels, 1991). The studies of Spiegler (1991) on Leg 114 material from the South Atlantic Ocean and those of Mackensen and Spiegler (1992) on Leg 120 material from the Kerguelen Plateau, southern Indian Ocean, suggest that the biostratigraphic utility of this group in the Southern Ocean may be improved further and may rival planktonic foraminifers. In addition, *Bolboforma* were identified at Site 1092 of Leg 177. The preparation methods used to obtain *Bolboforma* were the standard techniques used to obtain foraminifers (Mackensen and Spiegler, 1992). The occurrences of *Bolboforma* were designated as follows:

A = abundant (>25 specimens per 20 cm³).

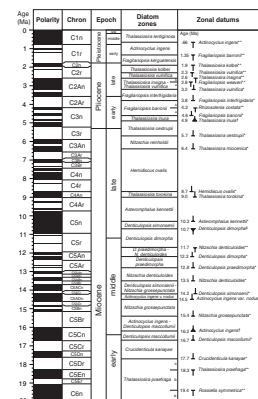
C = common (11–25 specimens per 20 cm³).

R = rare (<11 specimens per 20 cm³).

Diatoms

Numerous diatom biostratigraphic studies have been completed in Southern Ocean sediments (Gersonde and Burckle, 1990; Baldauf and Barron, 1991; Harwood and Maruyama, 1992; Gersonde and Bárcena, 1998). The Paleogene and Neogene diatom zonal scheme used during Leg 188 was primarily that proposed by Harwood and Maruyama (1992; Leg 120) (Fig. F8), with some modification. Some zone names were revised using the taxonomic transfer of genus *Nitzschia* to *Fragilariopsis* (Round et al., 1990; Hasle, 1993; Gersonde and Bárcena, 1998). Diatom workers on recent legs (Legs 177 and 178) removed the *Fragilariopsis kerguelensis* Zone because of taxonomic problems in distinguishing the last occurrence (LO) of *Fragilariopsis barronii*. This is because biostratigraphically younger *F. barronii* specimens can be mistaken for *F. kerguelensis* or *Fragilariopsis ritscherii*. The use of the *F. kerguelensis* Zone was retained for Leg 188, despite taxonomic problems associated with its upper boundary. Additionally, a new marker species, *Thalassiosira oliverana*, was adopted for the base of the *Nitzschia reinholdii* Zone for use during Legs 177 and 178. During Leg 188, we have retained the usage of the first occurrence (FO) of *Thalassiosira miocenica* for the base of this zone, as the first occurrence of *T. oliverana* most likely lies well below the FO of *T. miocenica*.

F8. Southern Ocean diatom zonal scheme plotted against the geomagnetic polarity time scale, p. 49.



All of the absolute ages for the marker species datums were recalculated to the Berggren et al. (1995b) time scale (Table T1), and the boundaries in the zonal scheme were repositioned accordingly. Several new diatom zones for the Pleistocene were established in a recent paper (Gersonde and Bárcena, 1998). The detailed diatom biostratigraphy of Gersonde and Bárcena (1998), however, was not used during this cruise because their scheme is derived from sections recovered in more northerly latitudes. Shipboard Scientific Party (1999b; Leg 177) pointed out that the FO of *Thalassiosira vulnifica*, which marks the base of the *Thalassiosira insigna*–*T. vulnifica* Zone of Harwood and Maruyama (1992), is a diachronous event in the Southern Ocean. They replaced this zone with the *T. insigna* Zone and divided it into Subzones a–c. These new subzones were defined wholly by the FO and LO of *T. insigna*. The range of *T. insigna*, however, is not well documented on the Antarctic margin; consequently, the *T. insigna*–*T. vulnifica* Zone definition of Harwood and Maruyama (1992) was retained for this study.

Figure F8 illustrates the diatom zonal scheme, paleomagnetic calibration, and marker species datums used during this leg. However, this zonation scheme was not fully applicable to the diatom flora in all the sediments recovered during Leg 188 because of the absence or low abundance of several marker species. Recent drilling in western McMurdo Sound, Ross Sea, at Cape Roberts resulted in the development of a new zonal scheme for the Antarctic continental shelf and the identification of numerous new taxa (Harwood et al., 1998; Scherer et al., in press). These new data were applied to lower Oligocene–upper Eocene sediments of Hole 1166A.

Reworking was noted in several Leg 188 samples. Biostratigraphic assignment of these samples was preferentially based upon FO datums over LO or last common occurrence (LCO) datums. Postcruise analyses will provide additional data that will help in delineating true ranges from reworked specimens.

Methods

Strewn slides from core-catcher samples were examined routinely for stratigraphic marker species. When required (in material with few specimens), selected samples were processed using hydrogen peroxide. Sieving (>10 µm) was also performed when necessary to remove excess clays and to break down biosiliceous clasts. Slides were routinely examined on a Zeiss compound microscope at 630× and 1000× magnification, with the higher power being reserved mainly for confirmation of identification.

Abundance of individual diatom taxa was based on the number of specimens observed per field of view at 630×. Diatom abundance estimates were recorded as follows:

- A = abundant (>10 valves per field of view).
- C = common (1–10 valves per field of view).
- F = few (≥1 valve per 10 fields of view and <1 valve per field of view).
- R = rare (≥3 valves per traverse of coverslip and <1 valve per 10 fields of view).
- X = present (<3 valves per traverse of coverslip, including an appearance as fragments).
- B = barren (no valves observed in slide).

T1. Oligocene to Pleistocene diatom zonal ages, p. 62.

Preservation was recorded as follows:

- E = excellent (nearly pristine, complete skeleton, lacking signs of dissolution, recrystallization, or breakage).
- G = good (majority of specimens complete; minor dissolution, recrystallization, and/or breakage).
- M = moderate (minor but pervasive dissolution, small amount of recrystallization, or breakage of specimens).
- P = poor (strong dissolution or recrystallization or breakage; many specimens unidentifiable).

PALEOMAGNETISM

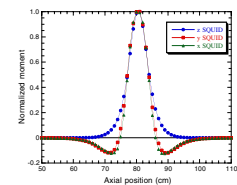
Paleomagnetic and rock magnetic investigations aboard the *JOIDES Resolution* during Leg 188 included routine measurements of natural and artificial remanent magnetizations of archive-half sections and discrete samples before and after static alternating field (AF) demagnetization, low-field magnetic susceptibility (k) measurements, and a limited set of rock magnetic measurements aimed at characterizing the down-core variation in the composition, concentration, and grain size of the magnetic carriers (e.g., Verosub and Roberts, 1995).

Shipboard Laboratory Facilities

The shipboard paleomagnetic laboratory is equipped with the following:

1. An automated pass-through cryogenic magnetometer manufactured by 2-G Enterprises (model 760-R) with an in-line, three-axis AF demagnetizer (2-G Enterprises model 2G600), capable of reaching peak fields of 80 mT at a frequency of 200 Hz. The sensing pickup coils measure the magnetic signal over an interval of ~ 7 cm (half-power width of the response curve), and the coils for each of the x-, y-, and z-axes have slightly different response curves (Fig. F10). The widths of the sensing regions correspond to <100 cm³ of cored material. This large volume within the sensing region permits accurate determination of remanent intensities as weak as $\sim 10^{-6}$ A/m, despite the relatively high background noise related to the motion of the ship. The background noise level of the magnetometer on board the *JOIDES Resolution* is $\sim 3 \times 10^{-6}$ A/m;
2. A Molspin Minispin spinner magnetometer capable of measuring higher remanent intensities than the 2-G magnetometer with some loss of accuracy, for use with strongly magnetized samples;
3. A DTECH alternating field demagnetizer (model D-2000) available for demagnetization of discrete samples of rock or sediment. The unit can demagnetize five samples simultaneously at peak alternating fields of up to 200 mT. The D-2000 can also be used to impart an anhysteretic remanent magnetization (ARM), in which a direct-current (DC) magnetic field is produced continuously across the AF demagnetizer coil, or a partial ARM (pARM), in which the user selects the demagnetization interval over which the field is applied;

F10. Comparison of the response curves for the shipboard cryogenic superconducting DC-SQUID magnetometer, p. 54.



4. A Schonstedt Instrument Co. thermal demagnetizer (model TSD-1) capable of demagnetizing discrete samples to 800°C with a resolution and repeatability of ~1°C. The residual magnetic field inside the TSD-1 was measured using a three-axis fluxgate magnetometer (model APS 520). The mean magnetic field within the furnace chamber is 99 nT with a minimum of 27 nT at 35 cm from the external door of this chamber. Within the cooling chamber, the residual magnetic field has a mean value of 8 nT and a minimum of 4 nT at 90 cm from the furnace chamber door (Fig. F11). During the thermal demagnetization, samples were arranged in the center of the heating and cooling regions to obtain magnetic fields <100 nT during heating and <5 nT during cooling. The samples were inserted in alternate directions at each heating step to check for spurious magnetizations acquired during the thermal demagnetization experiments;
5. An Analytical Services Company model IM-10 impulse magnetizer capable of applying magnetic fields from 0.02 to 1.35 T to study stepwise and saturation isothermal remanent magnetization of discrete samples;
6. A Bartington MS2 susceptibility meter, with a dual frequency sensor, operating at 0.565 and 5.650 kHz to measure low-field susceptibility at two frequencies; and
7. An Agico KLY-2.03 Kappabridge (KLY2) magnetic susceptibility meter with an operating frequency of 920 Hz and a magnetic induction of 0.3 mT. This instrument has a sensitivity of 1×10^{-6} SI units. The KLY2 operates at a single frequency and is particularly sensitive to the high background noise levels caused by the ship's motion.

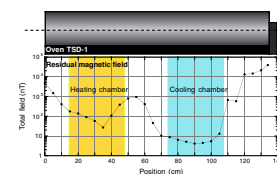
Measurement Procedure

The bulk of the remanence measurements made during Leg 188 were carried out using the shipboard pass-through cryogenic magnetometer. The standard ODP magnetic coordinate system was used (+x: vertical upward from the split surface of archive halves; +y: left along split surface when looking upcore; +z: downcore) (Fig. F12).

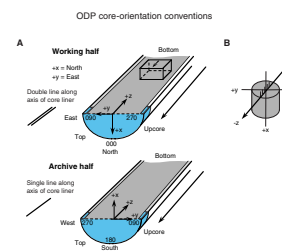
Natural remanent magnetization was routinely measured on all archive-half sections at 4-cm intervals with 15-cm-long headers and trailers. Measurements at core and section ends and within intervals of drilling-related core deformation were removed during data processing. AF demagnetizations were applied to cores at 10, 20, and 30 mT. The low maximum peak demagnetization fields ensured that the archive halves remain useful for shore-based high-resolution (U-channels) studies of magnetic properties.

Discrete samples were collected from the working halves in standard 8-cm³ plastic cubes with the arrow on the bottom of the sampling cube pointing upcore (-z). Our preferred strategy was to sample from the working halves at an interval of one meter; whenever possible, samples were selected from fine-grained horizons. Intervals with drilling-induced core deformation were avoided. The discrete samples were analyzed on the shipboard pass-through cryogenic magnetometer using a tray designed for measuring six discrete samples. Samples were AF demagnetized using the in-line demagnetizer installed on the pass-through cryogenic magnetometer at steps of 0, 10, 20, 30, 40, 50, 60, 70, and 80 mT. A subset of samples was thermally demagnetized using the Schonstedt TSD-1 oven. All of the samples subjected to thermal de-

F11. Total magnetic field measured inside the TSD-1 oven with a fluxgate magnetometer, p. 55.



F12. Core-orientation conventions for split core and discrete cylindrical sample, p. 56.



magnetization were measured at steps of 0°, 100°, 200°, 300°, 330°, 360°, 400°, 500°, 550°, 600°, 650°, and 700°C. The samples were heated for 90 min at the first demagnetization step to ensure that they had fully dried, then for 40 min at each subsequent step to ensure that they had reached thermal equilibrium. After each step, the low-field magnetic susceptibility was measured to monitor for thermal alteration.

Magnetic susceptibility was measured for each whole-core section as part of the MST (see “Physical Properties,” p. 21) using a Bartington MS2 meter coupled to an MS2C sensor coil with a diameter of 88 cm, operating at 0.565 kHz. The sensor was set on SI units, and the data were stored in the Janus database in raw meter units. The sensor coil is sensitive over an interval of ~4 cm (half-power width of the response curve) (Fig. F13), and the width of the sensing region corresponds to a volume of 166 cm³ of cored material. To convert to true SI volume susceptibilities, these values were multiplied by 10⁻⁵ and then multiplied by a correction factor to take into account the volume of material that passed through the susceptibility coils. Except for measurements near the ends of each section, the correction factor for a standard full ODP core is ~0.67 (= 1/1.5). The end effect of each core section was not corrected.

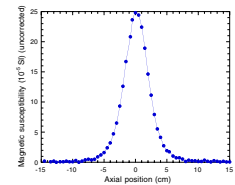
The low-field magnetic susceptibility was also routinely measured for all the discrete samples, and the data were compared with the whole-core susceptibility log. The frequency-dependent susceptibility, $fd(\%) = 100 \times (k_{low} - k_{high})/k_{low}$ was monitored to estimate the contribution of superparamagnetic contamination (Bloemendal et al., 1985). Measurements of k_{high} , however, were sometimes unstable and gave unusually high $fd(\%)$ values or negative values.

Further analyses were made on a selected subset of discrete samples. These analyses included the determination of the following:

1. Stepwise acquisition of isothermal remanent magnetization (IRM) in fields up to 1.3 T;
2. Coercivity of remanence (B_{cr}) and S-ratio ($-IRM_{-0.3T}/IRM_{1.3T}$) (e.g., Bloemendal et al., 1992; Verosub and Roberts, 1995) determined by progressively increasing the backfield up to 300 mT to the maximum IRM;
3. ARMs imparted by using a 100-mT AF and a 0.05-mT DC bias field; and
4. Stepwise thermal demagnetization of a composite IRM (Lowrie, 1990) at steps of 0°, 100°, 200°, 300°, 330°, 360°, 400°, 500°, 550°, 600°, 650°, and 700°C. Fields of 1.3, 0.5, and 0.12 T were applied along the x-, y-, and z-axes of a sample to distinguish between high-, intermediate-, and low-coercivity magnetic phases, respectively. After each thermal demagnetization step, the low-field magnetic susceptibility was measured to monitor for thermally induced phase changes.

Estimates of the concentration of magnetic minerals can be obtained from parameters such as k , IRM, and ARM, whereas B_{cr} , S-ratio, and thermomagnetic curves are more diagnostic of magnetic mineral composition.

F13. Response curve for the magnetic susceptibility loop on the MST position, p. 57.



Magnetostratigraphy

Where magnetic cleaning successfully isolated the characteristic component of magnetization (ChRM), paleomagnetic inclinations were used to define magnetic polarity zones. Interpretations of the magnetic polarity stratigraphy, with constraints from the biostratigraphic data, are presented in the site chapters. The revised time scale of Cande and Kent (1992, 1995), as presented in Berggren et al. (1995a, 1995b), was used as a reference for the ages of Cenozoic polarity chrons.

INORGANIC GEOCHEMISTRY

Interstitial Water Sampling and Chemistry

Shipboard interstitial water analyses for Leg 188 were performed on 5- to 20-cm whole-round sediment sections, which were cut and capped immediately after the core arrived on deck. Before squeezing, the outside surface of each whole-round section was carefully removed with a spatula to minimize potential contamination. Whole rounds were placed into a titanium and stainless steel squeezing device and squeezed at ambient temperature by applying pressure up to 40,000 lb (~4150 psi) with a hydraulic press (Manheim and Sayles, 1974). Interstitial water was extruded through a prewashed Whatman no. 1 filter fitted above a titanium screen. All interstitial water samples were filtered through 0.45-mm Gelman polysulfone disposable filters and collected into clean plastic syringes. After collection of up to 30 mL of interstitial water, the syringe was removed, a fresh 0.45-mm Gelman filter was attached, and aliquots were dispensed into plastic vials for shipboard analyses and into acid-washed plastic vials and 5-mL glass ampoules (heat sealed) for future shore-based work.

Interstitial water analyses followed the procedures outlined by Gieskes et al. (1991). Interstitial water samples were routinely analyzed for salinity with a Goldberg optical hand-held refractometer (Reichert), yielding a unitless approximate value for the concentration of dissolved solids. Alkalinity was measured by Gran titration with a Brinkmann pH electrode and a Metrohm autotitrator, and pH was measured on the National Institute of Standards scale as part of the alkalinity titration. It should be noted that pH measurements obtained in this fashion are not always reliable, given that the algorithm employed for pH measurement before the start of the alkalinity titration is adversely influenced by degassing. Dissolved chloride (Cl^-) was determined by titration with AgNO_3 . Dissolved silica (H_4SiO_4), ammonium (NH_4^+), and phosphate (PO_4^{3-}) concentrations were determined by spectrophotometric methods with a Milton Roy Spectronic 301 spectrophotometer (Gieskes et al., 1991). International Association for the Physical Sciences of the Ocean standard seawater was used for calibrating most techniques. The reproducibility of these analyses, determined by repeated measurements of standards, are alkalinity, <1.5%; Cl^- , <0.3%; H_4SiO_4 , <3%; PO_4^{3-} and NH_4^+ , ~3%. Calcium (Ca^{2+}), magnesium (Mg^{2+}), potassium (K^+), and sulfate (SO_4^{2-}) were measured to within 3%–5% on 1/200 diluted aliquots in nanopure water using a Dionex DX-120 ion chromatograph.

Lithium (Li^+), manganese (Mn^{2+}), and strontium (Sr^{2+}) were quantified by inductively coupled plasma-atomic emission spectrometry (ICP-

AES) with a Jobin-Yvon JY2000. Tenfold dilutions of the interstitial water sample were used for all of the elemental analyses by ICP-AES. Standards for all ICP-AES techniques were matrix matched as closely as possible to samples using filtered surface seawater that had been spiked with the appropriate concentrations of specific elements and serially diluted according to the method outlined by Murray et al. (in press). Both accuracy and precision are generally better than 1%–2% for these elements. All of the chemical data are reported in molar concentration units.

ORGANIC GEOCHEMISTRY

The shipboard organic geochemistry program for Leg 188 included four routine sets of analyses: (1) headspace analysis for volatile hydrocarbons as required by ODP safety regulations; (2) measurement of inorganic carbon content of the sediments; (3) elemental analyses of total carbon, total nitrogen, and total sulfur content of sediment; and (4) characterization of organic matter by Rock-Eval pyrolysis. Procedures and instruments used during Leg 188 are described by Emeis and Kvenvolden (1986) and generally are the same as those used during most recent ODP legs. Brief comments on routine sampling and deviations from standard practice are noted below; more detailed notes are presented in the “Explanatory Notes” chapters of the Leg 150, 155, and 164 *Initial Reports* volumes (Shipboard Scientific Party, 1994, 1995, and 1996, respectively).

Hydrocarbon Gases

The composition of gases evolved from the sediment was determined at least once for every core. Visible void spaces in the core liner were sampled by syringe and analyzed for gas composition. The primary headspace sampling technique analyzed the gas given off by a known quantity of sediment after heating in an airtight vial.

Two gas chromatography (GC) systems were used for the gas analysis: a Hewlett-Packard 5890 Series II GC and a Hewlett-Packard 5890A natural gas analyzer. The Series II GC determines concentrations of C₁ (methane), C₂ (ethane), and C₃ (propane) hydrocarbons with a flame ionization detector (FID). The natural gas analyzer measures concentrations of C₁ through C₇ hydrocarbons with an FID as well as N₂, O₂, and CO₂ with a thermal conductivity detector. For both systems, the chromatographic response was calibrated to standard gas mixtures.

Inorganic Carbon and Carbonate

Inorganic carbon (IC) content of sediment samples was determined by coulometry. Carbonate content of sediment (in weight percent) was calculated from IC content by assuming that all carbonate is present as calcium carbonate (CaCO₃):

$$\text{CaCO}_3 = \text{IC} \times 8.33.$$

Total carbon, nitrogen, and sulfur contents of sediment samples were determined with a Carlo Erba NCS analyzer. Total organic carbon (TOC)

content was calculated as the difference between total carbon (TC) and IC:

$$\text{TOC} = \text{TC} - \text{IC}.$$

Organic Matter Characterization

Type and quality of organic matter in sediment were evaluated by Rock-Eval pyrolysis. In this procedure, the volatile hydrocarbon content (in milligrams per gram) released by heating at 300°C for 3 min is called S_1 . The hydrocarbons produced by pyrolysis as the temperature is increased from 300° to 600°C at a heating rate of 25°C/min is called S_2 . CO_2 (in milligrams per gram) generated between 300° and 390°C is called S_3 . The nominal temperature of the maximum rate of hydrocarbon yield during S_2 analysis is T_{max} . TOC is calculated from S_1 , S_2 , and S_3 and from the oxidation of the remaining carbon in the sediment sample. The carbon-normalized hydrogen index (HI; in milligrams of hydrocarbon per gram of carbon) and the oxygen index (OI; in milligrams of carbon dioxide per gram of carbon) were calculated from the pyrolysis values:

$$\text{HI} = (100 \times S_2)/\text{TOC} \text{ and}$$

$$\text{OI} = (100 \times S_3)/\text{TOC}.$$

PHYSICAL PROPERTIES

The primary goals of physical properties measurements during Leg 188 were (1) to examine variations in physical properties related to the variations in sediment composition (thus, depositional history) on the continental rise, slope, and shelf of Prydz Bay; (2) to provide data sets to aid in the interpretation of seismic reflection and downhole geophysical measurements; and (3) to determine a preliminary stress history. Initial measurements of physical properties were undertaken on the MST after the cores had equilibrated to ambient temperature 3–4 hr after recovery. These nondestructive measurements were performed on unsplit, 1.5-m-long sections. The MST combines four sensors on an automated track to measure bulk density by gamma-ray attenuation, P -wave velocity, magnetic susceptibility, and natural gamma-ray emission. The MST provides a nearly continuous physical properties record; however, the quality of the data is highly dependent upon the condition of the core. Where possible, thermal conductivity was measured at intervals of one or two per core on whole-round sections. The cores were then split, and undrained shear strength and longitudinal and transverse P -wave velocity were measured on the working half. The moisture and density (MAD) measurements determined on discrete samples were dry density, bulk density, grain density, water content, porosity, and void ratio. Usually, one to two samples per section were taken from the same position as the discrete velocity measurements except where lithology or time dictated otherwise. Thermal conductivity was measured on pieces of split core in cases where measurements had not been possible on the whole-round core and where there was an intact piece of sufficient length. Physical properties data were transferred

to the ODP database from the computer systems controlling the MST and index properties sensors.

Moisture and Density Measurements

Samples of ~10 cm³ volume were taken for determination of MAD. Bulk density, grain density, water content, porosity, and dry density were calculated from wet and dry sample weights and dry volumes. Masses were measured with a Scitech electronic balance (precision = 0.1%). The balance was connected to a computer with weight-averaging software that corrected for ship accelerations. The sample mass was counterbalanced by a reference mass such that the mass differences were generally <2 g. Sample volumes were determined using a Quantachrome Penta-Pycnometer, a helium-displacement pycnometer with a precision of ±0.04 cm³. Sample volumes were determined as many as three times. A standard reference volume was run with each group of samples during the measurements and rotated among the measurement cells to check for instrument drift and systematic error. A purge time of 3 min was used before each run. The sample beakers used for discrete determinations of index properties were calibrated before the cruise. Dry weight and volume measurements were performed after the samples were oven dried at 105 ± 5°C for 24 hr and allowed to cool in a desiccator. Water content, bulk density, porosity, grain density, dry density, and void ratio were determined following the procedures and equations outlined in Blum (1997). The procedures for the determination of water content comply with the American Society for Testing and Materials (ASTM) designation D2216 (ASTM, 1990). Bulk density, grain density, and porosity were computed from the wet and dry masses and the dry volume of the sample using Method C of Blum (1997).

Multisensor Track

The GRA bulk densiometer allows an estimation of wet bulk density by measuring the attenuation of gamma rays passing through the cores, where the degree of attenuation is proportional to density (Boyce, 1976; Gerland and Villinger, 1995). Calibration of the system was carried out using a known freshwater/aluminum density standard with four components of different average densities. Density measurements were taken at 2- to 4-cm intervals with counting times of 2 s.

The *P*-wave logger (PWL) transmits a 500-kHz compressional wave pulse through the core at a rate of 1 kHz. The transmitting and receiving transducers are aligned perpendicular to the core axis. An average of 50 traveltime determinations was taken. A displacement transducer monitors the separation between the compressional wave transducers, so that variations in the outside diameter of the liner do not degrade the accuracy of the velocities. The PWL does not provide accurate velocity values if there is no acoustic coupling between the sediment and the liner and is therefore most useful in undisturbed APC cores. Measurements were taken at 2- to 4-cm intervals. Calibration of the displacement transducer and measurement of electronic delay within the PWL circuitry was carried out using a series of acrylic blocks of known thickness and *P*-wave traveltime. The validity of the calibration was checked by measuring the *P*-wave velocity through a section filled with distilled water.

Whole-core magnetic susceptibility was measured at 4-cm intervals on a Bartington MS2C meter with an 80-mm (internal diameter) loop

sensor using the 1.0 (1 s integration time) range and averaging five readings. Susceptibility values were archived in raw instrument units, which require multiplication by a factor of 6.6×10^{-6} to convert to volume-normalized SI units.

The area of influence for the four natural gamma-ray (NGR) sensors is $\sim\pm 10$ cm from the points of measurements along the core axis. The installation and operating principles of the NGR system are discussed by Blum (1997). Data from 256 energy channels were collected and archived. Total counts have been summed up over the range from 200 to 3000 keV to be comparable with data collected during previous legs. Measurements were made at 12-cm intervals. No corrections were made to account for incompletely filled core liners. The calibration procedure consisted of tuning all four scintillation counters to the same signal level for a particular emission energy, using the potassium peak; measuring background radiation caused by impurities in the system; and making an energy calibration by measuring standards with characteristic emission peaks at known energies (see Blum, 1997).

The accuracy of GRA bulk density, PWL, and magnetic susceptibility measurements degrades considerably in APC and XCB sections with gas voids or where the core otherwise does not fill the liner completely or is disturbed.

Velocimetry

In addition to the velocity measurements with the PWL, compressional wave velocity, V_p , was measured on split-core sections with the digital sound velocimeter using two types of piezoelectric transducer pairs (*P*-wave sensors 1 and 2 [PWS1 and PWS2]). The transducers were inserted into soft sediments along (*z*-direction [PWS1]) and orthogonal (*y*-direction [PWS2]) to the core axis. Velocity calculation is based on the fixed distance between the transducers (7.0 and 3.5 cm, respectively), measurement of the traveltime of an acoustic impulse, and a delay constant determined by measuring a water standard. The velocity meter was calibrated by measuring V_p in distilled water. In indurated sediments, a modified Hamilton frame velocimeter (PWS3) was used, which measured the traveltime of a 500-kHz signal orthogonally across the split-core section and core liner (*x*-direction) (Blum, 1997). In addition to traveltimes, sample thickness was measured using a digital micrometer that is zeroed periodically. In cases where the core was sufficiently indurated, block samples were trimmed, and velocities were measured in the *x*-, *y*-, and *z*-directions using PWS3.

Velocity data recorded in the Janus database are uncorrected for in situ temperature and pressure. These corrections can be made using the relationships given in Wylie et al. (1956), Wilson (1960), and Mackenzie (1981).

Undrained Shear Strength

The undrained shear strength, C_u , of the sediment was determined using three methods: the ODP motorized miniature vane shear device, a pocket penetrometer, and a fall-cone device provided for Leg 188 by one of the shipboard scientists.

The motorized miniature vane shear device was run in soft sediments following the procedures of Boyce (1977). The instrument measures the torque and rotation at the vane shaft using a torque transducer and po-

tentiometer, respectively. The shear strength reported is the peak strength determined from the torque vs. rotation plot. In addition to the peak shear strength, the residual strength was determined from the same plot if the failure was not dominated by cracking of the sample (Pyle, 1984). In the analysis of vane tests, it is assumed that a cylinder of sediment is uniformly sheared around the axis of the vane in an undrained condition with cohesion as the principal contributor to shear strength. Departures from this assumption include progressive cracking within and outside the failing specimen, uplift of the failing core cylinder, drainage of local pore pressures (i.e., the test can no longer be considered undrained), and stick-slip behavior. The pocket penetrometer measurements were converted from kilograms per square centimeter to kilopascals and then divided by two, as the penetrometer was calibrated as an unconfined compression test (for the ideal clay) equal to twice the undrained shear strength (Holtz and Kovacs, 1981). A small adapter point was provided by one of the shipboard scientific party for sediments with strengths in the range of 200 to 900 kPa.

The fall-cone device (Skempton and Bishop, 1950) provides a rapid and simple method for determination of undrained shear strength for undisturbed (as well as remolded) clays. A cone of known weight and apex angle is lowered to touch the sediment surface. After release, it penetrates into the sediment only by its own weight. Based on empirical relationships, the penetration can be directly converted to undrained shear strength in kilopascals. The results are usually the average of three measurements. Four different cones were used: 10 g/30°, 60 g/60°, 100 g/30°, and 400 g/30°, covering the shear strength intervals of 0.1–1.5 kPa, 2.2–9.0 kPa, 18–88 kPa, and 55–370 kPa, respectively. Fall-cone measurements affect a smaller volume of sediment during the measurement and are therefore less affected by sand- and gravel-sized material than the vane shear measurements. Fracturing of the sediment, which is the main cause of error in the vane shear measurements, is also avoided using the fall-cone device.

Thermal Conductivity

The TK04 (Teka, Berlin) was used for thermal conductivity measurements. A full-space needle probe was used for unconsolidated sediments, and a half-space needle was used for lithified sediments. The full-space needle probe, containing a heater wire and a calibrated thermistor, was inserted into the sediment through a small hole drilled into the core liner. The half-space needle was attached to a section of split core, and the assembly was immersed in seawater. Initially, Velcro straps were used to attach the needle, but it was later found that elastic bands provided a more secure attachment. Three measuring cycles were automatically performed at each location with the full-space needle and four cycles with the half-space needle. At the beginning of each test, a self-test, which included a drift study, was conducted. Once the samples were equilibrated, the heater circuit was closed and the temperature rise in the probes was recorded. Thermal conductivities were calculated from the rate of temperature rise while the heater current was flowing. Temperatures measured during the first 150 s of the heating cycle were fitted to an approximate solution of a constantly heated line source (Kristiansen, 1982; see Blum, 1997, for details). Errors are between 5% and 10%. Corrections were not attempted for in situ temperature or pressure effects.

IN SITU TEMPERATURE MEASUREMENTS

Temperature measurements were taken at two Prydz Bay drill sites (Sites 1165 and 1167) to determine the downhole and areal variation in heat flow and thermal gradient. The discrete measurements were made with the temperature tool, which is located in the coring shoe of the APC, during piston-coring operations. The components include a platinum temperature sensor and a data logger. The platinum resistance temperature device is calibrated for temperatures ranging from -20° to 100°C , with a resolution of 0.01°C . In operation, the adapted coring shoe is mounted on a regular APC barrel and lowered down the pipe by wireline. The tool is typically held for 5–10 min in the mudline to equilibrate with bottom-water temperatures and then lowered to the bottom of the drill string. Standard APC techniques are used, with the core barrel being fired into the sediment using hydraulic pressure. The Adara temperature tool (and APC barrel) remains in the sediment for 10–15 min to obtain a temperature record. This provides a sufficiently long transient record for extrapolation to a steady-state temperature. The nominal accuracy of the temperature measurement is $\sim 0.1^{\circ}\text{C}$.

These temperature data were then combined with the measured thermal conductivity data from the core samples (see “[Physical Properties](#),” p. 21) to calculate the heat flow and thermal gradients at each site. Assuming a predominantly conductive thermal regime, the heat flow can be determined by plotting the measured temperature vs. thermal resistance of the sedimentary section (Langseth and Takami, 1992). Fourier’s Law for one-dimensional vertical heat conduction can be expressed by

$$Q = k(dT/dZ),$$

where Q = heat flow (mW/m^2), k = thermal conductivity ($\text{W}/[\text{m}\cdot^{\circ}\text{C}]$), and (dT/dZ) is the thermal gradient ($^{\circ}\text{C}/\text{km}$). If a steady-state system is assumed and Q is constant with depth, then Q can be combined with measured conductivity to give an expression of temperature variation with depth over the entire intersected sedimentary section:

$$T_i = T_o + Q \int (dZ/k) = T_o + \{Q \sum_i 2[(Z_{i+1} - Z_i)/(k_{i+1} - k_i)]\} / 1000,$$

where T_i = the temperature ($^{\circ}\text{C}$) at depth Z_i (m), T_o = seafloor temperature, and k_i = the discrete measured thermal conductivity ($\text{W}/[\text{m}\cdot^{\circ}\text{C}]$).

DOWNHOLE MEASUREMENTS

Introduction

Downhole logs are used to determine physical, chemical, and structural properties of the formation penetrated by a borehole. The data are rapidly collected, continuous with depth, and measured in situ; they can be interpreted in terms of the stratigraphy, lithology, mineralogy, and geochemical composition of the penetrated formation. Where core recovery is incomplete or disturbed, log data may provide the only way to characterize the borehole section; where core recovery is good, log and core data complement one another and may be interpreted jointly. Downhole logs are sensitive to formation properties on a scale that is

intermediate between those obtained from laboratory measurements on core samples and geophysical surveys. They are useful in calibrating the interpretation of geophysical survey data (e.g., through the use of synthetic seismograms) and provide a necessary link for the integrated understanding of physical properties on all scales. Wireline logging was planned for all three sites, with logging while drilling (LWD) planned for the upper sections of the shelf and fan sites.

Wireline Logging

During wireline logging, the logs are made with a variety of Schlumberger logging tools combined into several “tool strings,” which are run down the hole after coring operations are complete. Four wireline tool strings were used during Leg 188: the triple combination (triple combo) (resistivity, density, and porosity); the Formation MicroScanner (FMS)-sonic (resistivity image of the borehole wall and sonic velocities); the geological high-resolution magnetic tool (GHMT)-sonic (magnetic field strength, magnetic susceptibility, and sonic velocities) and the FMS alone (Fig. F14; Table T3).

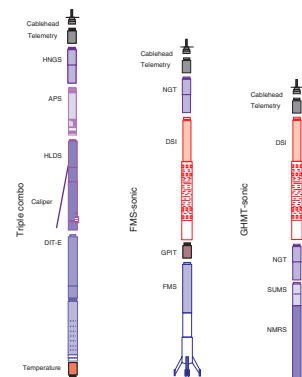
Each tool string also contains a telemetry cartridge for communicating through the wireline to the Schlumberger Minimum Configuration Maxis (MCM) unit on the drillship and a natural gamma radiation tool that provides a common reference for correlation and depth shifting between multiple logging runs. Logging runs are typically conducted at 250–275 m/hr.

In preparation for logging, the boreholes were flushed of debris by circulating a “pill” of viscous drilling fluid (sepiolite mud mixed with seawater; approximate weight = 8.8 lb/gal or 1.11 g/cm³) through the drill pipe to the bottom of the hole. The bottom-hole assembly (BHA) was pulled up to a depth of between 30 and 100 mbsf, then run down to the bottom of the hole again to ream borehole irregularities. The hole was subsequently filled with more sepiolite mud, and the pipe was raised to 30–100 mbsf and kept there to prevent hole collapse during logging. The tool strings were then lowered downhole by a seven-conductor wireline cable during sequential runs. A wireline heave compensator (WHC) was employed to minimize the effect of ship’s heave on the tool position in the borehole (Goldberg, 1990). During each logging run, incoming data were recorded and monitored in real time on the MCM logging computer. The tool strings were then pulled up at constant speed to provide continuous measurements as a function of depth of several properties simultaneously.

Logging While Drilling and Measurement While Drilling

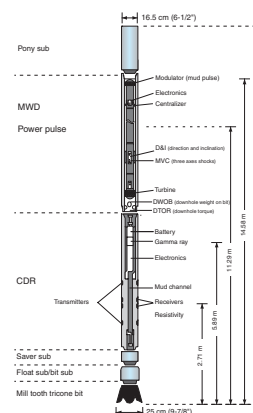
LWD measures in situ formation properties with instruments that are located in the drill collars immediately above the drill bit (Fig. F15). Measurements are made shortly after the hole is cut and before it is adversely affected by continued drilling or coring operations. Fluid invasion into the borehole wall is also reduced relative to wireline logging because of the shorter time between drilling and measurement. LWD has been successfully conducted during four previous ODP legs (Leg 156: Shipley, Ogawa, Blum, et al., 1995; Leg 170: Silver, Kimura, Blum, et al., 1998; Leg 171A: Moore, Klaus, et al., 1998; and Leg 174A: Austin, Christie-Blick, Malone, et al., 1998). The key difference between LWD

F14. Wireline tool strings used during Leg 188, p. 58.



T3. Wireline tool strings used during Leg 188, p. 64.

F15. Schematic diagram of the LWD BHA., p. 59.



and measurement while drilling (MWD) is that whereas LWD data are recorded in memory and downloaded when the tools reach the surface, MWD data are transmitted up the pipe by means of a pressure wave (mud pulsing) at 3 bits/s and monitored in real time. The term LWD is also used more generically to cover both LWD and MWD.

LWD operations were planned for the shelf and fan sites in the upper sections where core recovery had been poor on previous Antarctic ODP legs and that were too shallow for wireline logs to be made. A 40-m LWD hole was drilled at the shelf site, and a 261.1-m LWD hole was drilled at the fan site. Coring is not possible with an LWD BHA.

Two Schlumberger-Anadrill tools were used, the compensated dual resistivity tool (CDR; resistivity and spectral gamma ray) and the Power Pulse MWD tool. Figure F15 shows the configuration of the LWD BHA, and Table T4 lists the main set of measurements. A more detailed description of the LWD tools and their applications for ODP may be found in Moore, Klaus, et al. (1998), Schlumberger (1993), and Desbrandes (1994).

The LWD equipment is battery powered and uses erasable/programmable read-only memory chips (EPROM) to store the logging data until it is downloaded. The CDR takes measurements at evenly spaced time intervals and is synchronized with a system on the rig that monitors time and drilling depth. After drilling, the LWD tools were brought back to the drill floor and the data were downloaded from each tool through an RS232 serial link to a personal computer. The data were put onto a depth scale.

In addition to the CDR, the Power Pulse MWD tool was also run. The MWD tool makes several measurements, including downhole weight on bit and downhole torque, that are transmitted to the surface and not recorded in memory.

The weight on drawworks, drilling parameters, and pressure at the rig floor was digitally recorded using the Fusion instrumentation system. Together with the Anadrill rig-floor instrumentation and the downhole weight-on-bit information, the quality of the rig-floor data could be assessed as well as the efficacy of the passive heave compensation on the actual weight on bit.

LWD logs were provided by Schlumberger-Anadrill Drilling Services under contract with the Lamont-Doherty Earth Observatory Borehole Research Group (LDEO-BRG).

Logged Sediment Properties and Tool Measurement Principles

The logged properties, and the methods that the tools use to measure them, are briefly described below. The operating principles, applications, and approximate vertical resolution of the tools are summarized in Table T3. Some of the principal data channels of the tools, their physical significance, and measurement units are listed in Table T5. More detailed information on individual tools and their geological applications may be found in Ellis (1988), Goldberg (1997), Lovell et al. (1998), Rider (1996), Schlumberger (1989, 1994), and Serra (1984, 1986, 1989).

Natural Radioactivity

Two wireline spectral gamma-ray tools were used to measure and classify natural radioactivity in the formation: the natural gamma-ray

T4. Acronyms used to describe LWD and MWD tools, p. 65.

T5. Acronyms used to describe wireline tool strings and tool names, p. 66.

tool (NGT) and the hostile environment natural gamma-ray sonde (HN GS). The NGT uses a sodium-iodide scintillation detector and five-window spectroscopy to determine concentrations of K (percent), Th (parts per million), and U (parts per million), the three elements whose isotopes dominate the natural radiation spectrum. The HN GS is similar to the NGT, but it uses two bismuth germanate scintillation detectors for a significantly improved tool precision. The HN GS filters out gamma-ray energies below 500 keV, eliminating sensitivity to bentonite or KCl in the drilling mud and improving measurement accuracy. Although the NGT response is sensitive to borehole diameter and the weight and concentration of bentonite or KCl present in the drilling mud, corrections for these effects are routinely made during processing at LDEO.

Density

Formation density was determined with the hostile environment lithodensity sonde (HLDS). The sonde contains a radioactive cesium (^{137}Cs) gamma-ray source (622 keV) and far and near gamma-ray detectors mounted on a shielded skid, which is pressed against the borehole wall by a hydraulically activated eccentricizing arm. Gamma rays emitted by the source undergo Compton scattering, which involves the transfer of energy from gamma rays to the electrons in the formation via elastic collision. The number of scattered gamma rays that reach the detectors is directly related to the number of electrons in the formation, which is in turn related to bulk density. Porosity may also be derived from this bulk density if the matrix density is known.

The HLDS also measures photoelectric absorption as the photoelectric effect (PEF). Photoelectric absorption of the gamma rays occurs when they reach <150 keV after being repeatedly scattered by electrons in the formation. As PEF depends on the atomic number of the elements in the formation, it also varies according to the chemical composition of the minerals present and is essentially independent of porosity. For example, the PEF of calcite = 5.08 barn/e⁻; illite = 3.03 barn/e⁻; quartz = 1.81 barn/e⁻; and kaolinite = 1.49 barn/e⁻. Good contact between the tool and borehole wall is essential for good HLDS logs; poor contact results in underestimation of density values.

Porosity

Formation porosity was measured with the accelerator porosity sonde. The sonde incorporates a minitron neutron generator that produces fast (14.4 MeV) neutrons and five neutron detectors (four epithermal and one thermal) positioned at different spacings from the minitron. The measurement principle involves counting neutrons that arrive at the detectors after being slowed by neutron absorbers surrounding the tool. The highest energy loss occurs when neutrons collide with hydrogen nuclei, which have practically the same mass as the neutron (the neutrons simply bounce off heavier elements without losing much energy). If the hydrogen (i.e., water) concentration is small, as in low-porosity formations, neutrons can travel farther before being captured and the count rates increase at the detector. The opposite effect occurs when the water content is high. However, because hydrogen bound in minerals such as clays or in hydrocarbons also contributes to the measurement, the raw porosity value is often an overestimate.

Upon reaching thermal energies (0.025 eV), the neutrons are captured by the nuclei of Cl, Si, B, and other elements, resulting in a gamma-ray emission. This neutron capture cross section (Σ_f) is also measured by the tool.

Electrical Resistivity

The phasor dual-induction/spherically focused resistivity tool (DIT) was used to measure electrical resistivity. The DIT provides three measures of electrical resistivity, each with a different depth of investigation into the formation. The two induction devices (deep and medium depths of penetration) transmit high-frequency alternating currents through transmitter coils, creating magnetic fields that induce secondary currents in the formation. These currents produce a new inductive signal, proportional to the conductivity of the formation, which is measured by the receiving coils. The measured conductivities are then converted to resistivity (in units of ohm-meters). For the shallow penetration resistivity, the current necessary to maintain a constant voltage drop across a fixed interval is measured; it is a direct measurement of resistivity. Sand grains and hydrocarbons are electrical insulators, whereas ionic solutions and clays are conductors. Electrical resistivity can therefore be used to evaluate porosity, fluid salinity, and the characteristics of the pore structure.

The CDR LWD tool broadcasts a 2-MHz electromagnetic wave and measures the phase shift and the attenuation of the wave between two receivers. These quantities are transformed into two independent resistivities that provide the two depths of investigation. The phase shift is transformed into a shallow resistivity; the attenuation is transformed into a deep resistivity.

Temperature, Acceleration, and Pressure

Downhole temperature, acceleration, and pressure were measured with the LDEO high-resolution temperature/acceleration/pressure (TAP) tool. When attached to the bottom of the triple combo string, the TAP is run in an autonomous mode with data stored in built-in memory. Two thermistors are mounted near the bottom of the tool to detect borehole fluid temperatures at different rates. A thin fast-response thermistor is able to detect small, abrupt changes in temperature. A thicker slow-response thermistor is used to estimate temperature gradients and thermal regimes more accurately. The pressure transducer is included to activate the tool at a specified depth. A three-axis accelerometer measures tool movement downhole, providing data for analyzing the effects of heave on a deployed tool string, which should eventually lead to the fine tuning of the WHC.

The temperature record must be interpreted with caution, as the amount of time elapsed between the end of drilling and the logging operation is generally not sufficient to allow the borehole to recover thermally from the influence of drilling fluid circulation. The data recorded under such circumstances may differ significantly from the thermal equilibrium of that environment. Nevertheless, from the spatial temperature gradient it is possible to identify abrupt temperature changes that may represent localized fluid flow into the borehole indicative of fluid pathways and fracturing and/or breaks in the temperature gradient that may correspond to contrasts in permeability at lithologic boundaries.

Acoustic Velocity

The dipole shear sonic imager measures the transit times between sonic transmitters and an array of eight receivers. It averages replicate measurements, thus providing a direct measurement of sound velocity through sediments that is relatively free from the effects of formation damage and enlarged borehole (Schlumberger, 1989). Along with the monopole transmitters found on most sonic tools, it also has two crossed dipole transmitters, which allow the measurement of shear wave velocity in addition to the compressional wave velocity, even in the slow formations typically encountered during ODP legs.

Formation MicroScanner

The FMS provides high-resolution electrical resistivity-based images of borehole walls. The tool has four orthogonal arms and pads, each containing 16 button electrodes that are pressed against the borehole wall during the recording (Fig. F16). The electrodes are arranged in two diagonally offset rows of eight electrodes each (Fig. F16). A focused current is emitted from the button electrodes into the formation, with a return electrode near the top of the tool. The intensity of current passing through the button electrodes is measured. Processing transforms these measurements, which reflect the microresistivity variations of the formation, into continuous spatially oriented high-resolution images that mimic the geologic structures of the borehole wall. Further processing can provide measurements of dip and direction (azimuth) of planar features in the formation.

The development of the FMS tool has added a new dimension to wireline logging (Luthi, 1990; Lovell et al., 1998; Salimullah and Stow, 1992). It has enabled the formation to be viewed in its complete state and often to be grouped into facies assemblages. Features such as bedding, fracturing, slump folding, and bioturbation can be resolved; the fact that the images are oriented means that fabric analysis can be carried out and bed orientations can be measured.

The maximum extension of the caliper arms is 15 in. In holes with a diameter larger than 15 in, the pad contact will be inconsistent, and the FMS images may be blurred. Irregular borehole walls will also adversely affect the images as contact with the wall is poor.

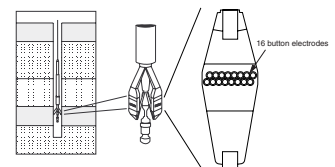
Accelerometry and Magnetic Field Measurement

Three-component acceleration and magnetic field measurements were made with the general-purpose inclinometer tool. The primary purpose of this tool, which incorporates a three-component accelerometer and a three-component magnetometer, is to determine the acceleration and orientation of the FMS-sonic tool string during logging. Thus, the FMS images can be corrected for irregular tool motion, and the dip and direction (azimuth) of features in the FMS image can be determined.

GHMT Tool String

The susceptibility measurement sonde (SUMS) measures magnetic susceptibility by means of low-frequency induction in the surrounding sediment. It responds primarily to magnetic minerals (mainly magne-

F16. Schematic diagram of the FMS, p. 61.



tites, hematite, and iron sulfides), which are typically contained in the detrital sediment fraction.

The nuclear resonance magnetometer sonde (NMRS) measures the total magnetic field using a proton precession magnetometer. The data from the SUMS and the NMRS tools can be used to construct a polarity stratigraphy, using the method outlined below.

The total magnetic field (B) measured in the borehole depends on position (p) and time (t) (Pozzi et al., 1988):

$$B(p,t) = B_r(p) + B_a(p) + B_t(p,t) + B_f(p),$$

where $B_f(p) = B_{fi}(p) + B_{fr}(p)$.

$B_r(p)$ is the Earth's main magnetic field, generated in the Earth's liquid outer core. The field intensity is ~50,000 nT for Prydz Bay. $B_a(p)$ is the magnetic field caused by the BHA (up to ~2000 nT, decaying away from the BHA) and crustal heterogeneities. $B_t(p,t)$ is the time-varying field (e.g., magnetic storms). Two passes of the GHMT are run to check that this is negligible. $B_{fi}(p)$ is the field produced in the borehole by the induced magnetization (J_i) of the sediment that is parallel to $B(p,t)$ and proportional to the magnetic susceptibility (χ): $J_i = B(p,t) \cdot \chi \cdot B_{fi}(p)$ is then given by $B_{fi}(p) = (J_i/2) \cdot (1 - 3\sin^2 l)$, where l is the inclination of the Earth's field at the site. $B_{fr}(p)$ is the field produced in the borehole by the remanent magnetization (J_r) of the sediment, whose polarity we aim to determine. J_r is either parallel (normal polarity) or anti-parallel (reversed polarity) to $B(p,t)$ if the site has not moved significantly (relative to the magnetic poles) since sediment deposition. We find $B_{fr}(p)$ by subtracting $B_r(p)$, $B_a(p)$, and $B_{fi}(p)$ from the total field measurement $B(p,t)$.

Under favorable conditions, a magnetostratigraphy is given simply by the sign of $B_{fr}(p)$. Further processing, completed onshore, involves regression analysis of $B_{fr}(p)$ vs. $B_{fi}(p)$ downhole on intervals of various thickness. Correlation indicates normal polarity, and anticorrelation indicates reversed polarity.

Log Data Quality

The principal influence on log data quality is the condition of the borehole wall. If the borehole diameter is variable over short intervals resulting from washouts during drilling, clay swelling, or borehole wall collapse, the logs from those tools that require good contact with the borehole wall (i.e., FMS, density, and porosity tools) may be degraded. Deep investigation measurements such as resistivity and sonic velocity, which do not require contact with the borehole wall, are generally less sensitive to borehole conditions. Very narrow ("bridged") sections will also cause irregular log results. The quality of the borehole is improved by minimizing the circulation of drilling fluid while drilling, flushing the borehole to remove debris, and logging as soon as possible after drilling and conditioning are completed.

Log Depth Scales

The depth of the wireline-logged measurement is determined from the length of the logging cable played out at the winch on the ship. The seafloor is identified on the natural gamma log by the abrupt reduction in gamma-ray count at the water/sediment boundary (mudline). In LWD, the logging depth is determined from the known length of the

BHA and pipe stands, the position of the top drive, and the stroke of the heave compensator (see Moore, Klaus, et al., 1998). The coring depth (driller's depth) is determined from the known length of the BHA and pipe stands; the mudline is usually recovered in the first core from the hole.

Discrepancies between the driller's depth and the wireline log depth occur because of core expansion, incomplete core recovery, incomplete heave compensation, and drill-pipe stretch in the case of drill-pipe depth; incomplete heave compensation, cable stretch (~1 m/km), and cable slip in the case of log depth. Tidal changes in sea level will also have an effect. To minimize the wireline tool motion caused by ship heave, a hydraulic wireline heave compensator adjusts for rig motion during wireline logging operations. The small but significant differences between drill-pipe depth and logging depth should be taken into account when using the logs for correlation with core and log measurements. Core measurements such as susceptibility and density can be correlated with the equivalent downhole logs using the Sagan program, which allows shifting of the core depths onto the log depth scale. Precise core-log depth matching is difficult in zones where core recovery is low because of the inherent ambiguity of placing the recovered section within the cored interval.

Logs from different wireline tool strings will have slight depth mismatches. Distinctive features recorded by the natural gamma tool, run on every tool string, provide correlation and relative depth offsets among the logging runs.

Data Recording and Processing

Data for each logging run were recorded, stored digitally, and monitored in real time using the MCM software. On completion of logging at each hole, data were transferred to the downhole measurements laboratory for preliminary interpretation. Basic processing was carried out postcruise to provide scientists with a comprehensive, quality-controlled downhole logging data set that can be used for comparison and integration with other data collected during each ODP leg. The processing includes depth adjustments to remove depth offsets between data from different logging runs; corrections specific to certain tools and logs; documentation for the logs, with an assessment of log quality; and conversion of the data to a widely accessible format (ASCII for the conventional logs; GIF for the FMS images). Schlumberger GeoQuest's GeoFrame software package is used for most of the processing. Post-cruise processing of FMS and GHMT log data was performed at the Laboratoire de Mesures en Forage, in Aix-en-Provence, France.

Processed acoustic, caliper, density, gamma-ray, magnetic, neutron porosity, resistivity, and temperature data in ASCII format are available (see the "[Related Leg Data](#)" contents list). A summary of logging highlights is also posted on the LDEO-BRG Web site (see "[Related Leg Data](#)" contents list) shortly after the end of each leg.

Core-Log-Seismic Integration

The IESX seismic interpretation software package was tested during Leg 188. It was used to display site-survey seismic sections acquired pre-cruise as well as the seismic section acquired from the *JOIDES Resolution* during the cruise. Velocity and density logs were used to create synthetic seismograms, which were overlaid on the seismic section and

used to refine the depth-traveltime relation. In this way, lithostratigraphic units in the core are correlated with reflectors and sequences in the seismic section.

REFERENCES

- Abelmann, A., 1992. Early to middle Miocene radiolarian stratigraphy of the Kerguelen Plateau, Leg 120. In Wise, S.W., Jr., Schlich, R., et al., *Proc. ODP, Sci. Results*, 120: College Station, TX (Ocean Drilling Program), 757–783.
- ASTM, 1990. Standard method for laboratory determination of water (moisture) content of soil and rock. In *Annual Book of ASTM Standards* (Vol. 04.08): Philadelphia (Am. Soc. Testing and Mater.), D 2216–90 (revision of 2216–63, 2216–80).
- Austin, J.A., Jr., Christie-Blick, N., Malone, M.J., et al., 1998. *Proc. ODP, Init. Repts.*, 174A: College Station, TX (Ocean Drilling Program).
- Baldauf, J.G., and Barron, J.A., 1991. Diatom biostratigraphy: Kerguelen Plateau and Prydz Bay regions of the Southern Ocean. In Barron, J., Larsen, B., et al., *Proc. ODP, Sci. Results*, 119: College Station, TX (Ocean Drilling Program), 547–598.
- Balsam, W.L., and Damuth, J.E., 2000. Further investigations of shipboard vs. shore-based spectral data: implications for interpreting Leg 164 sediment composition. In Paull, C.K., Matsumoto, R., Wallace, P., and Dillon, W.P. (Eds.), *Proc. ODP, Init. Repts.*, 164: College Station, TX (Ocean Drilling Program), 313–324.
- Balsam, W.L., Damuth, J.E., and Schneider, R.R., 1997. Comparison of shipboard vs. shore-based spectral data from Amazon Fan cores: implications for interpreting sediment composition. In Flood, R.D., Piper, D.J.W., Klaus, A., and Peterson, L.C. (Eds.), *Proc. ODP, Sci. Results*, 155: College Station, TX (Ocean Drilling Program), 193–215.
- Balsam, W.L., Deaton, B.C., and Damuth, J.E., 1998. The effects of water content on diffuse reflectance measurements of deep-sea core samples: an example from ODP Leg 164 sediments. *Mar. Geol.*, 149:177–189.
- , 1999. Evaluating optical lightness as a proxy for carbonate content in marine sediment cores. *Mar. Geol.*, 161:141–153.
- Barron, J.A., Baldauf, J.G., Barrera, E., Caulet, J.-P., Huber, B.T., Keating, B.H., Lazarus, D., Sakai, H., Thierstein, H.R., and Wei, W., 1991. Biochronologic and magneto-chronologic synthesis of Leg 119 sediments from the Kerguelen Plateau and Prydz Bay, Antarctica. In Barron, J., Larsen, B., et al., *Proc. ODP, Sci. Results*, 119: College Station, TX (Ocean Drilling Program), 813–847.
- Berggren, W.A., 1992a. Neogene planktonic foraminifer magnetobiostratigraphy of the southern Kerguelen Plateau (Sites 747, 748, and 751). In Wise, S.W., Jr., Schlich, R., et al., *Proc. ODP, Sci. Results*, 120 (Pt. 2): College Station, TX (Ocean Drilling Program), 631–647.
- , 1992b. Paleogene planktonic foraminifer magnetobiostratigraphy of the Southern Kerguelen Plateau (Sites 747–749). In Wise, S.W., Jr., Schlich, R., et al., *Proc. ODP, Sci. Results*, 120 (Pt. 2): College Station, TX (Ocean Drilling Program), 551–568.
- Berggren, W.A., Hilgen, F.J., Langereis, C.G., Kent, D.V., Obradovich, J.D., Raffi, I., Raymo, M.E., and Shackleton, N.J., 1995a. Late Neogene chronology: new perspectives in high-resolution stratigraphy. *Geol. Soc. Am. Bull.*, 107:1272–1287.
- Berggren, W.A., Kent, D.V., and Flynn, J.J., 1985. Jurassic to Paleogene, Part 2. Paleogene geochronology and chronostratigraphy. In Snelling, N.J. (Ed.), *The Chronology of the Geological Record*. Geol. Soc. London Mem., 10:141–195.
- Berggren, W.A., Kent, D.V., Swisher, C.C., III, and Aubry, M.-P., 1995b. A revised Cenozoic geochronology and chronostratigraphy. In Berggren, W.A., Kent, D.V., Aubry, M.-P., and Hardenbol, J. (Eds.), *Geochronology, Time Scales and Global Stratigraphic Correlation*. Spec. Publ.[0151] Soc. Econ. Paleontol. Mineral. (Soc. Sediment. Geol.), 54:129–212.
- Bloemendal, J., Barton, C.E., and Radhakrishnamurthy, C., 1985. Correlation between Rayleigh loops and frequency-dependent and quadrature susceptibility: application to magnetic granulometry of rocks. *J. Geophys. Res.*, 90:8789–8792.

- Bloemendal, J., King, J.W., Hall, F.R., and Doh, S.-J., 1992. Rock magnetism of late Neogene and Pleistocene deep-sea sediments: relationship to sediment source, diagenetic processes, and sediment lithology. *J. Geophys. Res.*, 97:4361–4375.
- Blum, P., 1997. Physical Properties Handbook: a Guide to the Shipboard Measurements of Physical Properties of Deep-sea Cores. *ODP Tech. Note*, 26.
- Boyce, R.E., 1976. Definitions and laboratory techniques of compressional sound velocity parameters and wet-water content, wet-bulk density, and porosity parameters by gravimetric and gamma-ray attenuation techniques. In Schlanger, S.O., Jackson, E.D., et al., *Init. Repts. DSDP*, 33: Washington (U.S. Govt. Printing Office), 931–958.
- , 1977. Deep Sea Drilling Project procedures for shear strength measurement of clayey sediment using modified Wykeham Farrance laboratory vane apparatus. In Barker, P.F., Dalziel, I.W.D., et al., *Init. Repts. DSDP*, 36: Washington (U.S. Govt. Printing Office), 1059–1068.
- Cande, S.C., and Kent, D.V., 1992. A new geomagnetic polarity time scale for the Late Cretaceous and Cenozoic. *J. Geophys. Res.*, 97:13917–13951.
- , 1995. Revised calibration of the geomagnetic polarity timescale for the Late Cretaceous and Cenozoic. *J. Geophys. Res.*, 100:6093–6095.
- Caulet, J.-P., 1991. Radiolarians from the Kerguelen Plateau, Leg 119. In Barron, J., Larsen, B., et al., *Proc. ODP, Sci. Results*, 119: College Station, TX (Ocean Drilling Program), 513–546.
- Chen, P.-H., 1975. Antarctic radiolaria. In Hayes, D.E., Frakes, L.A., et al., *Init. Repts. DSDP*, 28: Washington (U.S. Govt. Printing Office), 437–513.
- Desbrandes, R., 1994. *Data Acquisition and Processing While Drilling*. Dept. Petrol. Eng., Louisiana State Univ.
- Ellis, D.V., 1987. *Well Logging for Earth Scientists*: New York (Elsevier).
- Emeis, K.-C., and Kvenvolden, K.A., 1986. Shipboard organic geochemistry on *JOIDES Resolution*. *ODP Tech. Note*, 7.
- Forsberg, C.F., Solheim, A., Elverhøi, A., Jansen, E., Channell, J.E.T., and Andersen, E.S., 1999. The depositional environment of the western Svalbard margin during the late Pliocene and the Pleistocene: sedimentary facies changes at Site 986. In Raymo, M.E., Jansen, E., Blum, P., and Herbert, T.D. (Eds.), *Proc. ODP, Sci. Results*, 162: College Station, TX (Ocean Drilling Program), 233–246.
- Gerland, S., and Villinger, H., 1995. Nondestructive density determination on marine sediment cores from gamma-ray attenuation measurements. *Geo-Mar. Lett.*, 15:111–118
- Gersonde, R., Abelmann, A., Burckle, L.H., Hamilton, N., Lazarus, D., McCartney, K., O'Brien, P., Spieß, V., and Wise, S.W., Jr., 1990. Biostratigraphic synthesis of Neogene siliceous microfossils from the Antarctic Ocean, ODP Leg 113 (Weddell Sea). In Barker, P.F., Kennett, J.P., et al., *Proc. ODP, Sci. Results*, 113: College Station, TX (Ocean Drilling Program), 915–936.
- Gersonde, R., and Bárcena, M.A., 1998. Revision of the late Pliocene-Pleistocene diatom biostratigraphy for the northern belt of the Southern Ocean. *Micropaleontology*, 44:84–98.
- Gersonde, R., and Burckle, L.H., 1990. Neogene diatom biostratigraphy of ODP Leg 113, Weddell Sea (Antarctic Ocean). In Barker, P.F., Kennett, J.P., et al., *Proc. ODP, Sci. Results*, 113: College Station, TX (Ocean Drilling Program), 761–789.
- Gieskes, J.M., Gamo, T., and Brumsack, H., 1991. Chemical methods for interstitial water analysis aboard *JOIDES Resolution*. *ODP Tech. Note*, 15.
- Goldberg, D., 1990. Test performance of the Ocean Drilling Program wireline heave motion compensator. *Sci. Drill.*, 1:206–209.
- , 1997. The role of downhole measurements in marine geology and geophysics. *Rev. Geophys.*, 35:315–342.
- Harwood, D.M., Bohaty, S.M., and Scherer, R.P., 1998. Lower miocene diatom biostratigraphy of the CRP-1 drillcore, McMurdo Sound, Antarctica. *Terra Antart.*, 5:499–514.

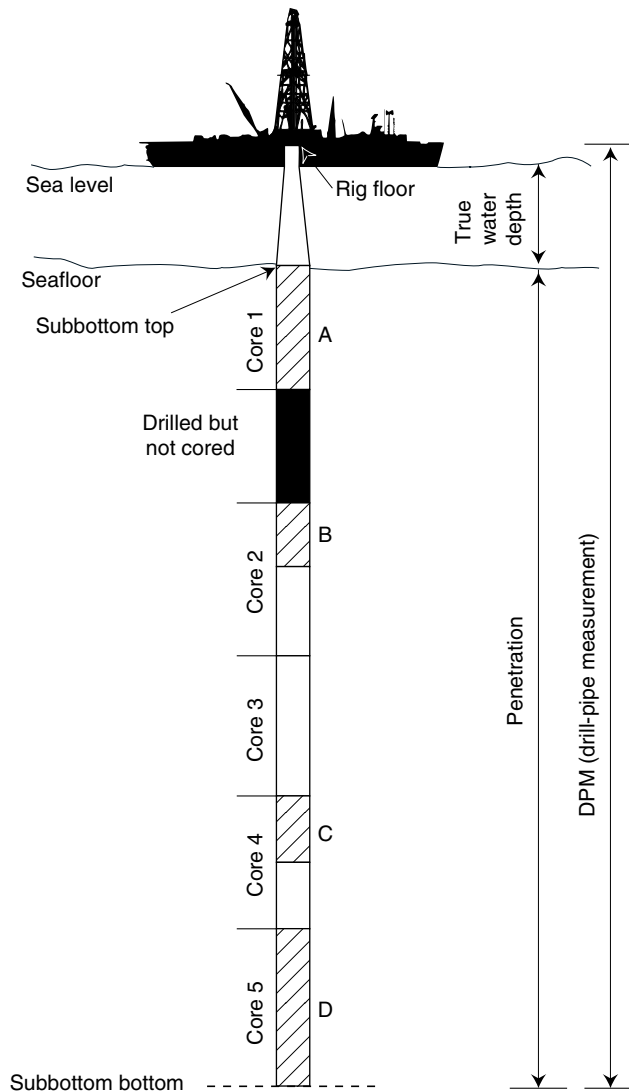
- Harwood, D.M., Lazarus, D.B., Abelmann, A., Aubry, M.-P., Berggren, W.A., Heider, F., Inokuchi, H., Maruyama, T., McCartney, K., Wei, W., and Wise, S.W., Jr., 1992. Neogene integrated magnetobiostratigraphy of the central Kerguelen Plateau, Leg 120. *In* Wise, S.W., Jr., Schlich, R., et al., *Proc. ODP, Sci. Results*, 120: College Station, TX (Ocean Drilling Program), 1031–1052.
- Harwood, D.M., and Maruyama, T., 1992. Middle Eocene to Pleistocene diatom biostratigraphy of Southern Ocean sediments from the Kerguelen Plateau, Leg 120. *In* Wise, S.W., Jr., Schlich, R., et al., *Proc. ODP, Sci. Results*, 120: College Station, TX (Ocean Drilling Program), 683–733.
- Hasle, G.R., 1993. Nomenclatural notes on marine planktonic diatoms. The family Bacillariaceae. *Nova Hedwigia. Beih.*, 106:315–321.
- Hays, J.D., 1965. Radiolaria and late Tertiary and Quaternary history of Antarctic seas. *In* Llano, G.A. (Ed.), *Biology of the Antarctic Seas II*. Antarct. Res. Ser., 5:125–184.
- Hollis, C.J., 1997. Cretaceous-Paleocene Radiolaria of eastern Marlborough, New Zealand. *Inst. Geol. Nucl. Sci. Monogr.*, 17.
- Holtz, R.D., and Kovacs, W.D., 1981. *An Introduction to Geotechnical Engineering*: Englewood Cliffs, NJ (Prentice-Hall).
- Huber, B.T., 1991. Paleogene and early Neogene planktonic foraminifer biostratigraphy of Sites 738 and 744, Kerguelen Plateau (southern Indian Ocean). *In* Barron, J., Larsen, B., et al., *Proc. ODP, Sci. Results*, 119: College Station, TX (Ocean Drilling Program), 427–449.
- Jenkins, D.G., and Srinivasan, M.S., 1986. Cenozoic planktonic foraminifers from the equator to the sub-antarctic of the southwest Pacific. *In* Kennett, J.P., von der Borch, C.C., et al., *Init. Repts. DSDP*, 90: Washington (U.S. Govt. Printing Office), 795–834.
- Johnson, D.A., Schneider, D.A., Nigrini, C.A., Caulet, J.-P., and Kent, D.V., 1989. Pliocene-Pleistocene radiolarian events and magnetostratigraphic calibrations for the tropical Indian Ocean. *Mar. Micropaleontol.*, 14:33–66.
- Keany, J., 1979. Early Pliocene radiolarian taxonomy and biostratigraphy in the Antarctic region. *Micropaleontology*, 25:50–74.
- Kristiansen, J.I., 1982. The transient cylindrical probe method for determination of thermal parameters of earth materials [Ph.D. dissert.]. Aarhus Univ.
- Langseth, M.G., and Tamaki, K., 1992. Geothermal measurements: thermal evolution of the Japan Sea basins and sediments. *In* Tamaki, K., Suyehiro, K., Allan, J., McWilliams, M., et al., *Proc. ODP, Sci. Results*, 127/128 (Pt. 2): College Station, TX (Ocean Drilling Program), 1297–1309.
- Lazarus, D., 1990. Middle Miocene to Recent radiolarians from the Weddell Sea, Antarctica, ODP Leg 113. *In* Barker, P.F., Kennett, J.P., et al., *Proc. ODP, Sci. Results*, 113: College Station, TX (Ocean Drilling Program), 709–727.
- , 1992. Antarctic Neogene radiolarians from the Kerguelen Plateau, Legs 119 and 120. *In* Wise, S.W., Jr., Schlich, R., et al., *Proc. ODP, Sci. Results*, 120: College Station, TX (Ocean Drilling Program), 785–809.
- Li, Q., and Radford, S.S., 1992. Morphology and affinity of the planktonic foraminifer *Cassigerinelloita amekiensis* Stolk and reclassification of *Cassigerinelloita* Stolk. *In* Wise, S.W., Jr., Schlich, R., et al., *Proc. ODP, Sci. Results*, 120: College Station, TX (Ocean Drilling Program), 595–602.
- Lovell, M.A., Harvey, P.K., Brewer, T.S., Williams, C., Jackson, P.D., and Williamson, G., 1998. Application of FMS images in the Ocean Drilling Program: an overview. *In* Cramp, A., MacLeod, C.J., Lee, S.V., and Jones, E.J.W. (Eds.), *Geological Evolution of Ocean Basins: Results from the Ocean Drilling Program*. Geol. Soc. Spec. Publ. London, 131:287–303.
- Lowrie, W., 1990. Identification of ferromagnetic minerals in a rock by coercivity and unblocking temperature properties. *Geophys. Res. Lett.*, 17:159–162.
- Luthi, S.M., 1990. Sedimentary structures of clastic rocks identified from electrical borehole images. *In* Hurst, A., Lovell, M.A., and Morton, A.C. (Eds.), *Geological Applications of Wireline Logs*. Geol. Soc. Spec. Publ. London, 48:3–10.

- Mackensen, A., and Berggren, W.A., 1992. Paleogene benthic foraminifers from the southern Indian Ocean (Kerguelen Plateau): biostratigraphy and paleoecology. *In* Wise, S.W., Jr., Schlich, R., et al., *Proc. ODP, Sci. Results*, 120: College Station, TX (Ocean Drilling Program), 603–630.
- Mackensen, A., and Spiegler, D., 1992. Middle Eocene to early Pliocene *Bolboforma* (algae?) from the Kerguelen Plateau, southern Indian Ocean. *In* Wise, S.W., Jr., Schlich, R., et al., *Proc. ODP, Sci. Results*, 120: College Station, TX (Ocean Drilling Program), 675–682.
- Mackenzie, K.V., 1981. Nine-term equation for sound speed in the oceans. *J. Acoust. Soc. Am.*, 70:807–812.
- Manheim, F.T., and Sayles, F.L., 1974. Composition and origin of interstitial waters of marine sediments, based on deep sea drill cores. *In* Goldberg, E.D. (Ed.), *The Sea* (Vol. 5): *Marine Chemistry: The Sedimentary Cycle*: New York (Wiley), 527–568.
- Martini, E., 1971. Standard Tertiary and Quaternary calcareous nannoplankton zonation. *In* Farinacci, A. (Ed.), *Proc. 2nd Int. Conf. Planktonic Microfossils Roma*: Rome (Ed. Tecnosci.), 2:739–785.
- Mazzullo, J.M., Meyer, A., and Kidd, R.B., 1988. New sediment classification scheme for the Ocean Drilling Program. *In* Mazzullo, J., and Graham, A.G. (Eds.), *Handbook for Shipboard Sedimentologists*. ODP Tech. Note, 8:45–67.
- Moncrieff, A.C.M., 1989. Classification of poorly-sorted sedimentary rocks. *Sediment. Geol.*, 64:191–194.
- Moore, J.C., Klaus, A., et al., 1998. *Proc. ODP, Init. Repts.*, 171A: College Station, TX (Ocean Drilling Program).
- Morely, J.J., and Nigrini, C., 1995. Miocene to Pleistocene radiolarian biostratigraphy of North Pacific Sites 881, 884, 885, 886, and 887. *In* Rea, D.K., Basov, I.A., Scholl, D.W., and Allan, J.F. (Eds.), *Proc. ODP, Sci. Results*, 145: College Station, TX (Ocean Drilling Program), 55–91.
- Munsell Color Company, Inc., 1975. *Munsell Soil Color Charts*: Baltimore, MD (Munsell).
- Murray, R.W., Miller, D.J., and Kryc, K.A., in press. Analysis of major and trace elements in rocks, sediments, and interstitial waters by inductively coupled plasma-atomic emission spectrometry (ICP-AES). *ODP Tech. Note*, 29.
- Okada, H., and Bukry, D., 1980. Supplementary modification and introduction of code numbers to the low-latitude coccolith biostratigraphic zonation (Bukry, 1973; 1975). *Mar. Micropaleontol.*, 5:321–325.
- Pospichal, J., Wei, W., and Wise, S.W., Jr., 1992. Probing the limits of nannofossil stratigraphic resolution in the Southern High Latitudes. *Mem. Sci. Geol.*, 43:115–131.
- Pozzi, P.-P., Martin, J.-P., Pocachard, J., Feinberg, H., and Galdeano, A., 1998. In-situ magnetostratigraphy; interpretation of magnetic logging in sediments. *Earth Planet Sci. Lett.*, 88:357–373.
- Pyle, M.R., 1984. Vane shear data on undrained residual strength. *J. Geotech. Engr. Div., Am. Soc. Civ. Eng.*, 110:543–547.
- Quilty, P.G., Truswell, E.M., O'Brien, P.E., and Taylor, F., 2000. Paleocene-Eocene biostratigraphy and palaeoenvironment of East Antarctica: new data from Mac. Robertson Shelf and the western parts of Prydz Bay. *AGSO J. Aust. Geol. Geophys.*, 17:133–143.
- Rider, M., 1996. *The Geological Interpretation of Well Logs* (2nd ed.): Caithness (Whittles Publishing).
- Round, F.E., Crawford, R.M., and Mann, D.G., 1990. *The Diatoms: Biology and Morphology of the Genera*: Cambridge (Cambridge Univ. Press).
- Salimullah, A.R.M., and Stow, D.A.V., 1992. Application of FMS images in poorly recovered coring intervals: examples from ODP Leg 129. *In* Hurst, A., Griffiths, C.M., and Worthington P.F. (Eds.), *Geological Application of Wireline Logs II*. Geol. Soc. Spec. Publ. London, 65:71–86.

- Scherer, R.P., Bohaty, S.M., and Harwood, D.M., in press. Oligocene and lower Miocene siliceous microfossil biostratigraphy of Cape Roberts Project core CRP-2/2A, Victoria Land Basin, Antarctica. *Terra Antart.*
- Schlumberger, 1989. *Log Interpretation Principles/Applications*: Houston, TX (Schlumberger Educ. Services).
- , 1993. *Logging While Drilling*: Houston, TX (Schlumberger Educ. Services), SMP-9160.
- , 1994. *IPL Integrated Porosity Lithology* (Schlumberger Wireline and Testing), SMP-9270.
- Serra, O., 1984. *Fundamentals of Well-Log Interpretation* (Vol. 1): *The Acquisition of Logging Data*: Dev. Pet. Sci., 15A: Amsterdam (Elsevier).
- , 1986. *Fundamentals of Well-Log Interpretation* (Vol. 2): *The Interpretation of Logging Data*. Dev. Pet. Sci., 15B.
- , 1989. *Formation MicroScanner Image Interpretation*: Houston (Schlumberger Educ. Services), SMP-7028.
- Shepard, F., 1954. Nomenclature based on sand-silt-clay ratios. *J. Sediment. Petrol.*, 24:151–158.
- Shipboard Scientific Party, 1987. Explanatory notes: ODP Leg 105, Baffin Bay and Labrador Sea. In Srivastava, S.P., Arthur, M., et al., *Proc. ODP, Init. Repts.*, 105: College Station, TX (Ocean Drilling Program), 21–42.
- , 1989. Explanatory notes. In Barron, J., Larsen, B., et al., *Proc. ODP, Init. Repts.*, 119: College Station, TX (Ocean Drilling Program), 15–44.
- , 1994. Explanatory notes. In Mountain, G.S., Miller, K.G., Blum, P., et al., *Proc. ODP, Init. Repts.*, 150: College Station, TX (Ocean Drilling Program), 21–42.
- , 1995. Explanatory notes. In Shipley, T.H., Ogawa, Y., Blum, P., et al., *Proc. ODP, Init. Repts.*, 156: College Station, TX (Ocean Drilling Program), 39–68.
- , 1996. Explanatory notes. In Paull, C.K., Matsumoto, R., Wallace, P., et al., *Proc. ODP, Init. Repts.*, 164: College Station, TX (Ocean Drilling Program), 13–41.
- , 1999a. Explanatory notes. In Carter, R.M., McCave, I.N., Richter, C., Carter, L., et al., *Proc. ODP, Init. Repts.* [CD-ROM], 181: College Station, TX (Ocean Drilling Program), 1–65.
- , 1999b. Explanatory notes. In Gersonde, R., Hodell, D.A., Blum, P., et al., *Proc. ODP, Init. Repts.* [CD-ROM], 177: College Station, TX (Ocean Drilling Program), 1–57.
- , 1999c. Site 1097. In Barker, P.F., Camenlenghi, A., Acton, G.D. et al., *Proc. ODP, Init. Reports* [CD-ROM], 178: College Station, TX (Ocean Drilling Program), 1–66.
- Shipley, T.H., Ogawa, Y., Blum, P., et al., 1995. *Proc. ODP, Init. Repts.*, 156: College Station, TX (Ocean Drilling Program).
- Silver, E., Kimura, G., Blum, P., et al., 1997. *Proc. ODP, Init. Repts.*, 170: College Station, TX (Ocean Drilling Program).
- Skempton, A.W., and Bishop, A.W., 1950. The measurement of shear strength of soils. *Geotechnique*, 2:90–108.
- Spiegler, D., 1991. Occurrence of *Bolboforma* (algae, Chrysophyta) in the subantarctic (Atlantic) Paleogene. In Ciesielski, P.F., Kristoffersen, Y., et al., *Proc. ODP, Sci. Results*, 114: College Station, TX (Ocean Drilling Program), 325–334.
- Spiegler, D., and von Daniels, C.H., 1991. A stratigraphic and taxonomic atlas of *Bolboforma* (Protophytes, incertae sedis, Tertiary). *J. Foraminiferal Res.*, 21:126–158.
- Stott, L.D., and Kennett, J.P., 1990. Antarctic Paleogene planktonic foraminifer biostratigraphy: ODP Leg 113, Sites 689 and 690. In Barker, P.F., Kennett, J.P., et al., *Proc. ODP, Sci. Results*, 113: College Station, TX (Ocean Drilling Program), 549–569.
- Takemura, A., 1992. Radiolarian Paleogene biostratigraphy in the southern Indian Ocean, Leg 120. In Wise, S.W., Jr., Shlich, R., et al., *Proc. ODP, Sci. Results*, 120: College Station, TX (Ocean Drilling Program), 735–756.

- Takemura, A., and Ling, H.Y., 1997. Eocene and Oligocene radiolarian biostratigraphy from the Southern Ocean: correlation of ODP Legs 114 (Atlantic Ocean) and 120 (Indian Ocean). *Mar. Micropaleontol.*, 30:97–116.
- Tappan, H., 1980. *The Paleobiology of Plant Protists*: San Francisco (W.H. Freeman).
- Verosub, K.L., and Roberts, A.P., 1995. Environmental magnetism: past, present, and future. *J. Geophys. Res.*, 100:2175–2192.
- Weaver, F.M., 1976. Antarctic Radiolaria from the southeast Pacific basin, Deep Sea Drilling Project, Leg 35. In Hollister, C.D., Craddock, C., et al., *Init. Repts. DSDP*, 35: Washington (U.S. Govt. Printing Office), 569–603.
- Wei, W., 1992. Paleogene chronology of Southern Ocean drill holes: an update. In Kennett, J.P., and Warnke, D.A. (Eds.), *The Antarctic Paleoenvironment: a Perspective on Global Change*. *Antarct. Res. Ser.*, 56:75–96.
- Wei, W., and Thierstein, H.R., 1991. Upper Cretaceous and Cenozoic calcareous nanofossils of the Kerguelen Plateau (southern Indian Ocean) and Prydz Bay (East Antarctica). In Barron, J., Larsen, B., et al., *Proc. ODP, Sci. Results*, 119: College Station, TX (Ocean Drilling Program), 467–494.
- Wei, W., and Wise, S.W., Jr., 1990. Middle Eocene to Pleistocene calcareous nanofossils recovered by Ocean Drilling Program Leg 113 in the Weddell Sea. In Barker, P.F., Kennett, J.P., et al., *Proc. ODP, Sci. Results*, 113: College Station, TX (Ocean Drilling Program), 639–666.
- , 1992a. Oligocene-Pleistocene calcareous nanofossils from Southern Ocean Sites 747, 748, and 751. In Wise, S.W., Jr., Schlich, R., et al., *Proc. ODP, Sci. Results*, 120: College Station, TX (Ocean Drilling Program), 509–521.
- , 1992b. Selected Neogene calcareous nanofossil index taxa of the Southern Ocean: biochronology, biometrics, and paleoceanography. In Wise, S.W., Jr., Schlich, R., et al., *Proc. ODP, Sci. Results*, 120: College Station, TX (Ocean Drilling Program), 523–537.
- Wentworth, C.K., 1922. A scale of grade and class terms of clastic sediments. *J. Geol.*, 30:377–392.
- Wilson, W.D., 1960. Speed of sound in seawater as a function of temperature, pressure and salinity. *J. Acoust. Soc. Am.*, 32:641–644.
- Wise, S.W., Jr., 1983. Mesozoic and Cenozoic calcareous nanofossils recovered by Deep Sea Drilling Project Leg 71 in the Falkland Plateau region, Southwest Atlantic Ocean. In Ludwig, W.J., Krasheninnikov, V.A., et al., *Init. Repts. DSDP*, 71 (Pt. 2): Washington (U.S. Govt. Printing Office), 481–550.
- Wyllie, M.R.J., Gregory, A.R., and Gardner, L.W., 1956. Elastic wave velocities in heterogeneous and porous media. *Geophysics*, 21:41–70.

Figure F1. Coring and depth intervals.



 Represents recovered material

Bottom felt: distance from rig floor to seafloor

Total depth: distance from rig floor to bottom of hole (subbottom bottom)

Penetration: distance from seafloor (subbottom top) to bottom of hole (subbottom bottom)

Number of cores: total of all cores recorded, including cores with no recovery

Total length

of cored section: distance from subbottom top to subbottom bottom minus drilled (but not cored) areas in between

Total core recovered: total from adding A, B, C, and D in diagram

Core recovery (%) = (Total core recovered/Total length of cored section) × 100

Figure F2. Examples of numbered core sections.

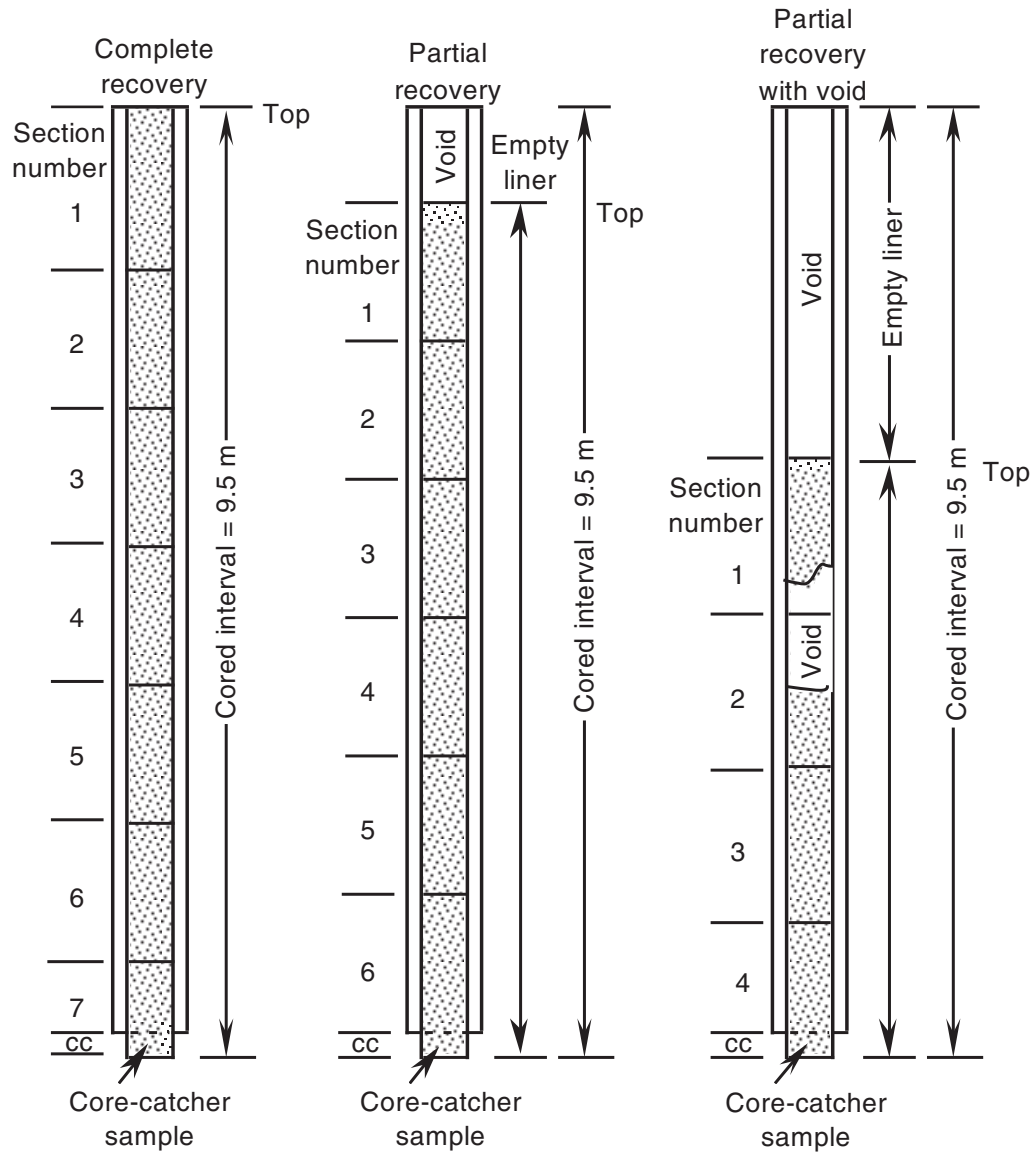


Figure F3. Key to symbols used to represent lithology, sedimentary structures, accessories, bioturbation, and drilling disturbance in the barrel sheets of Leg 188.

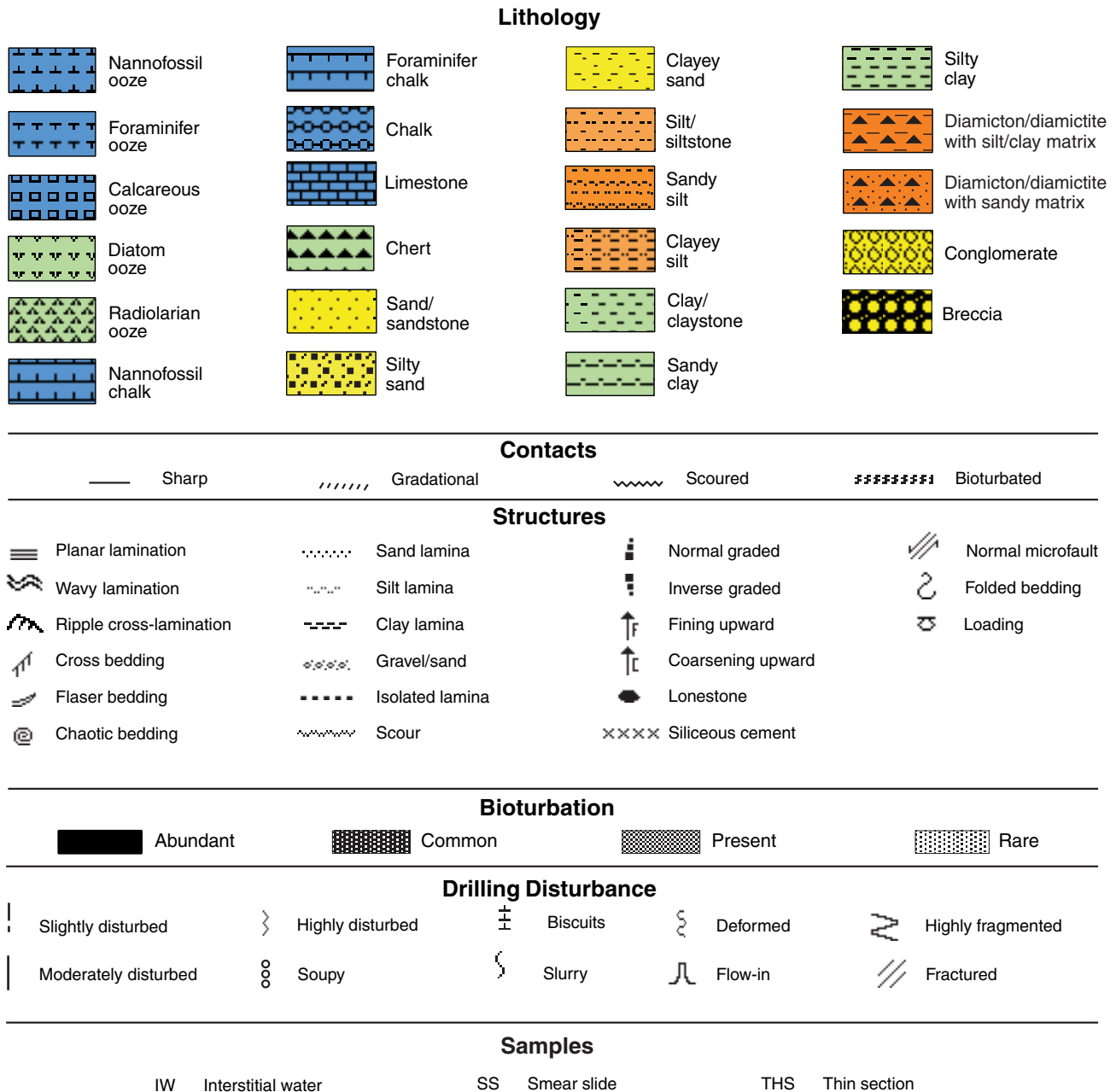


Figure F4. A. Textural classification scheme for siliciclastics, modified from Shepard (1954) by subdivision of the central triangular field into sandy clay, silty clay, sandy silt, clayey silt, clayey sand, and silty sand. The sand-, silt-, and clay-sized fractions are defined using the Wentworth (1922) grade scale. B. Procedure for naming mixtures of biogenic and siliciclastic sediments. In this scheme, the names shown for microfossil components and the siliciclastic fraction are examples only (i.e., placeholders) and can be replaced by any valid textural (for siliciclastic fraction) or microfossil name.

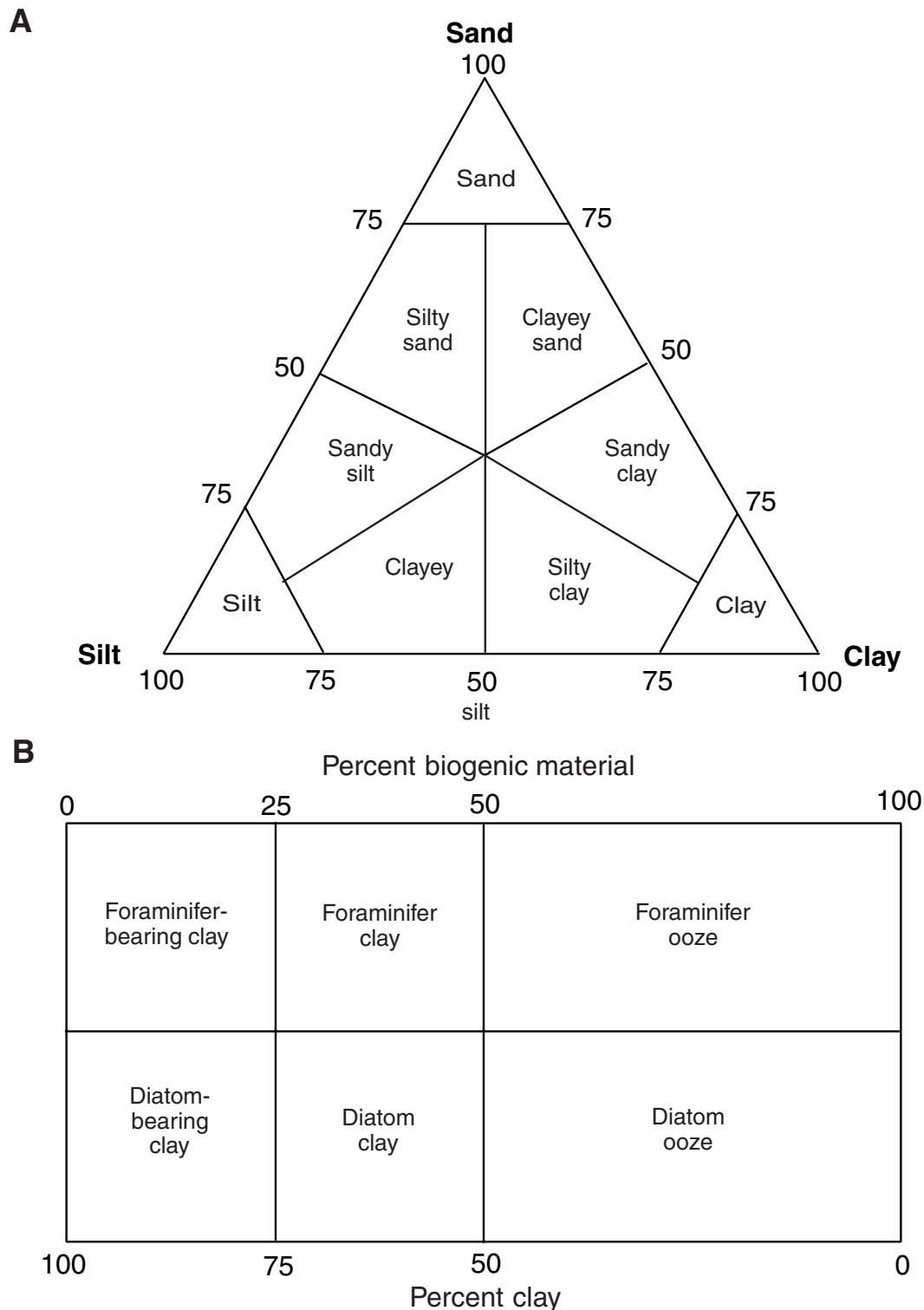


Figure F5. Classification of poorly sorted sediments with a gravel component to facilitate the characterization of diamicts, gravels/conglomerates, and breccias, modified after Moncrieff (1989). Matrix classification is based on Figure F4A, p. 43, and should be inserted at the asterisk. The terms *gravel* and *conglomerate* are used when most clasts are rounded and the term *breccia*, when most clasts are angular.

Percent gravel (>2 mm) in whole rock estimated from core

		Trace <5%	5%-10%	10%-30%	30%-80%	>80%
Percent sand in matrix	0	CLAY/SILT with dispersed clasts	CLAY/SILT with common clasts	CLAY/SILT with abundant clasts	clayey/silty GRAVEL/CONGLOMERATE/BRECCIA	GRAVEL/ CONGLOMERATE/ BRECCIA
	25	* CLAY/SILT with dispersed clasts	Clast-poor * DIAMICT	Clast-rich * DIAMICT	* GRAVEL/ CONGLOMERATE/ BRECCIA	
	50	* SAND with dispersed clasts	Clast-poor * DIAMICT	Clast-rich * DIAMICT	* GRAVEL/ CONGLOMERATE/ BRECCIA	
	75	SAND with dispersed clasts	SAND with common clasts	SAND with abundant clasts	sandy GRAVEL/CONGLOMERATE/BRECCIA	
100						

Figure F6. The X-ray unit mounted on a table in the entry area of the core laboratory.



Figure F7. Holocene through Paleogene time scale with foraminifer and nannofossil biostratigraphic datums used in this volume for the Prydz Bay drill sites (modified from Berggren et al., 1995b). High-latitude zonations used during Leg 188 vs. low-latitude zonations are indicated under “Leg 188” and “Low Lat.,” respectively. High-latitude biostratigraphic datum and age correlations are indicated in bold type under “Biostratigraphic Datums;” foraminiferal datums are underlined. Planktonic foraminifer zonations adopted from Berggren (1992b: Antarctic Neogene); Stott and Kennett (1990: Antarctic Paleogene; modified by Huber, 1991, and Berggren, 1992b). Nannofossil zonations adopted from Wise (1983: Antarctic Oligocene to mid-middle Eocene; modified by Wei and Wise, 1990, and Wei and Thierstein, 1991, and calibrated against magnetostratigraphy by Wei, 1992). **(Figure shown on next two pages.)**

Figure F7 (continued). (Caption shown on previous page.)

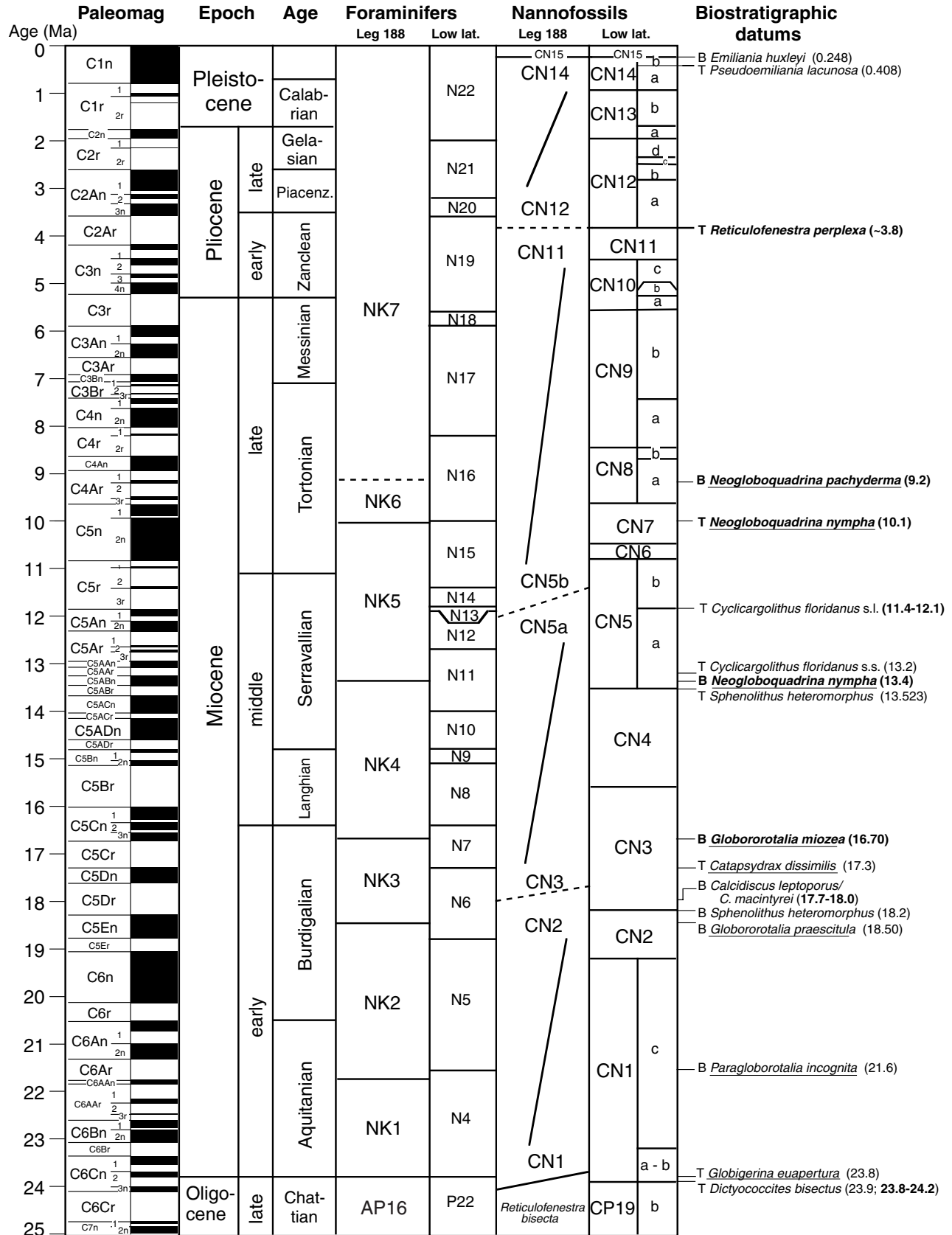


Figure F7 (continued).

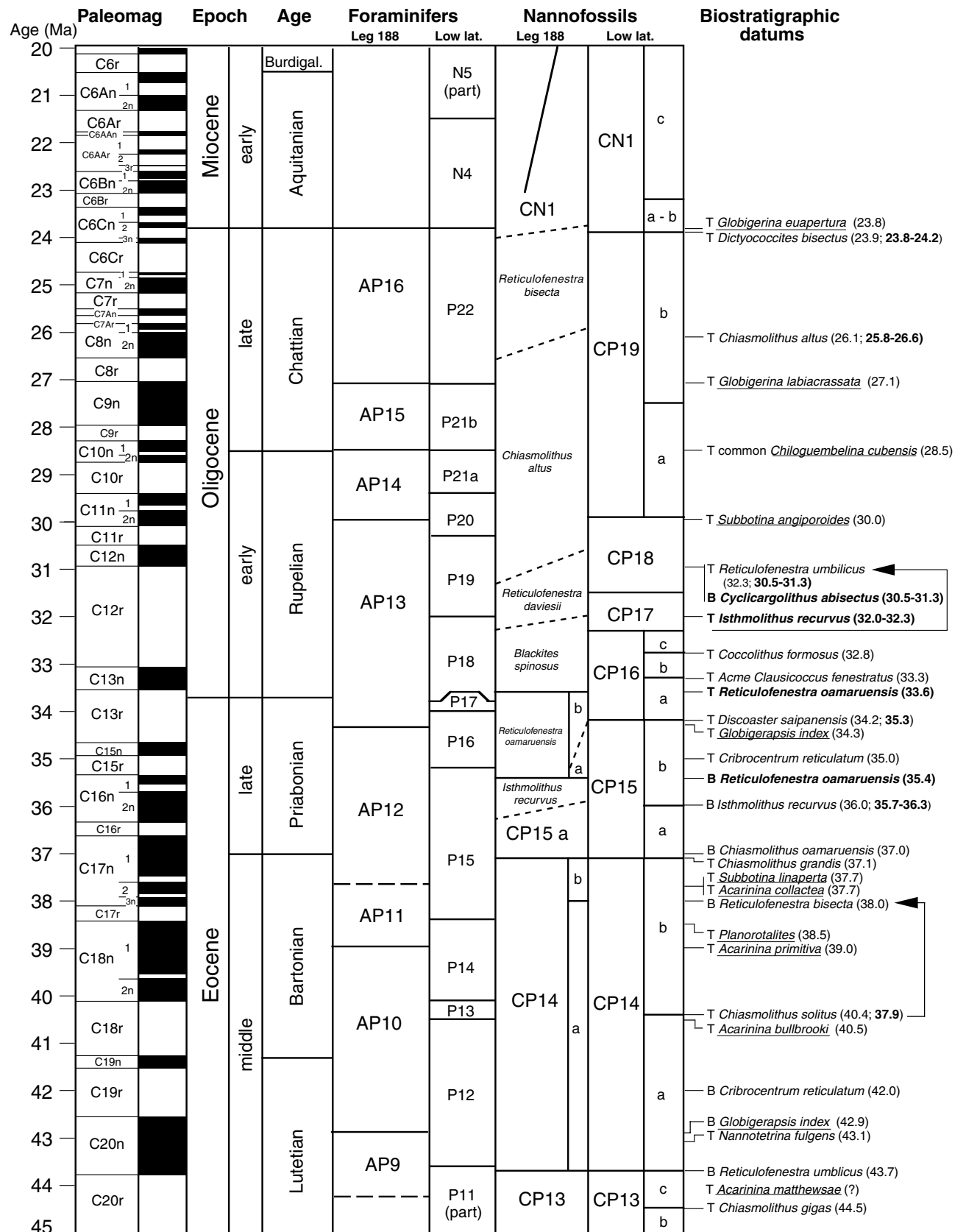


Figure F8. Southern Ocean diatom zonal scheme of Harwood and Maruyama (1992) plotted against the geomagnetic polarity time scale of Berggren et al. (1995b), 0–37 Ma interval. All zonal ages are revised from the Berggren et al. (1985) to the Berggren et al. (1995b) time scale. * = first occurrence, ** = last occurrence, † = first common occurrence, and ‡ = last common occurrence. (Continued on next page.)

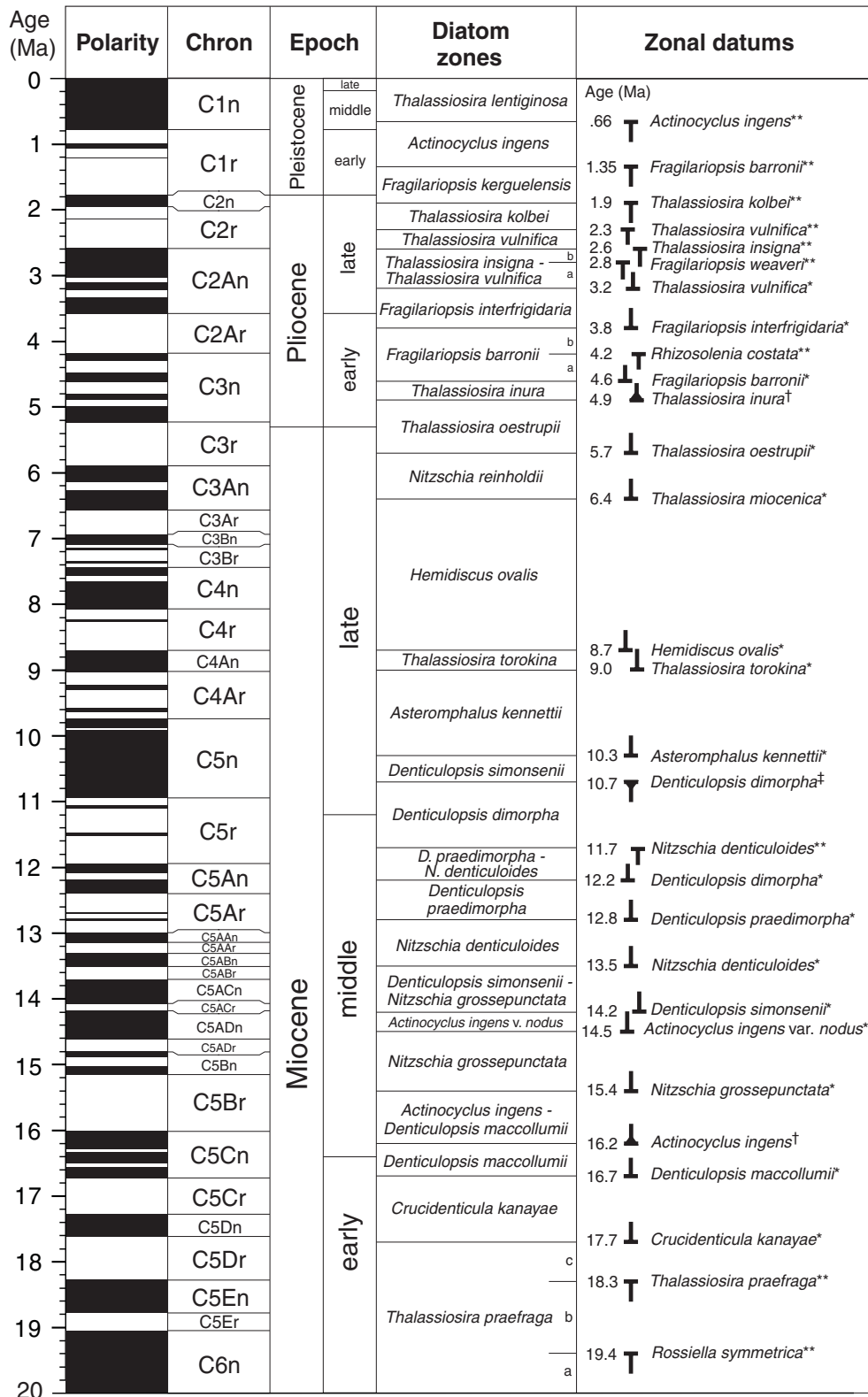


Figure F8 (continued).

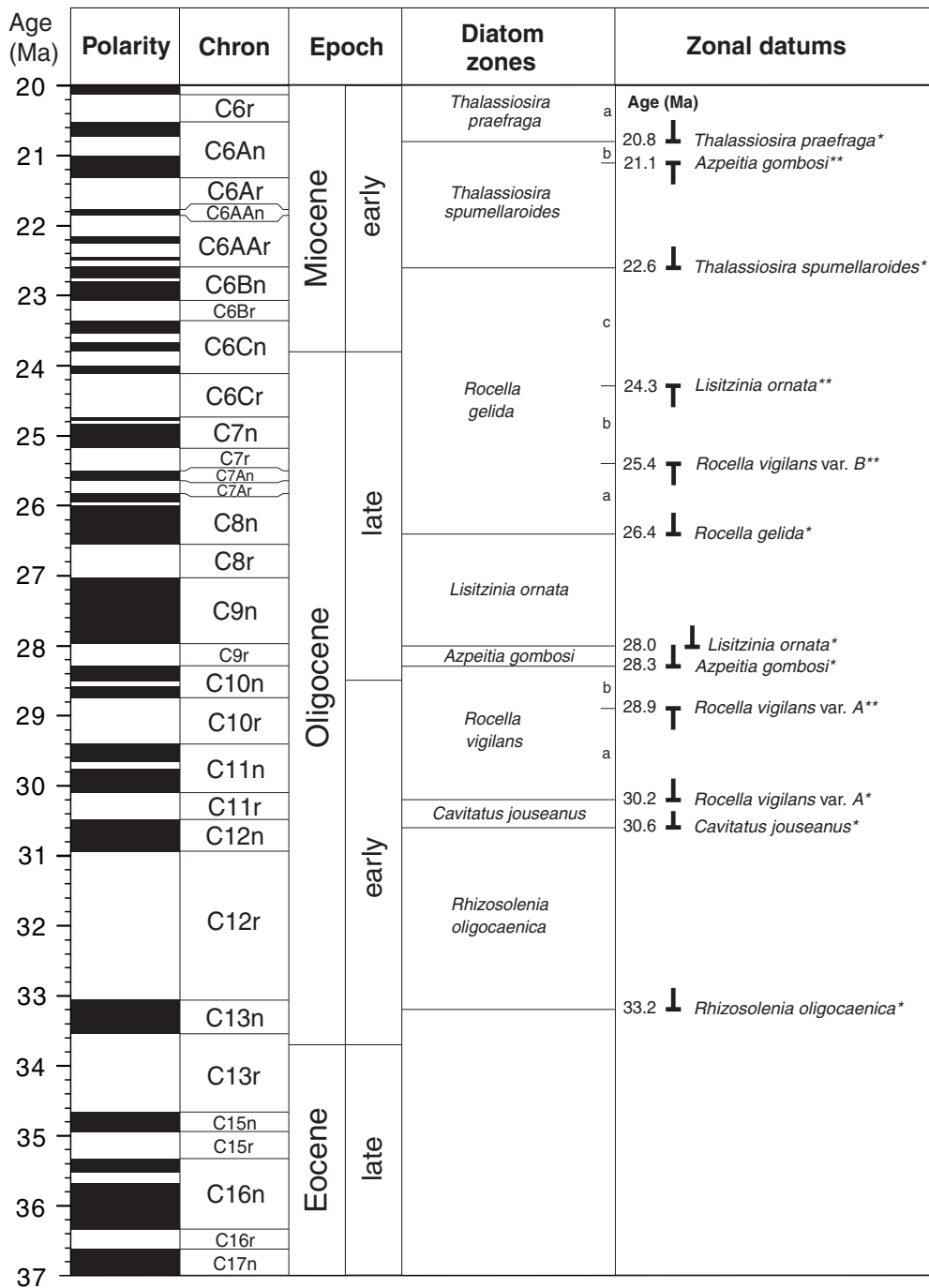


Figure F9. Cenozoic radiolarian biostratigraphic zonal schemes tied to the geomagnetic polarity time scale (Berggren et al., 1995b) and the New Zealand stages (Shipboard Scientific Party, 1999a). (Continued on next two pages.)

Age (Ma)	Chronos	Polarity	Epoch	Series	New Zealand		Ma	Lazarus(1992) Abelmann (1992) Antarctic/Subantarctic radiolarian zones	Inter- national	Sanfilippo and Nigrini (1998)		
					Stage	Ma				Code #	Tropical radiolarian zone	Ma
0.5	C1n	r	late		Haweran (Wq)	0.4	Omega	RN17	<i>Buccinosphaera invaginata</i>	0.18		
						0.46		RN16	<i>Collosphaera tuberosa</i>	0.42		
1	C1r	r	middle		Castlecliffian (Wc)	0.83	Psi	RN15	<i>Stylatractus universus</i>	0.61		
										RN14	<i>Amphirhopalum ypsilon</i>	~1.1
1.5	C2n	r	early		Nukumaruan (Wn)	1.6	Chi	RN13	<i>Anthocyrtidium angulare</i>	1.74		
2	C2r	r	late	Wanganui	Mangapanian (Wm)	1.9	Phi	RN12b	<i>Pterocanium prismatium</i>	2.4		
												RN12a
2.5	C2An	n	early		Waipipian (Wp)	2.4	Upsilon	RN11b	<i>Lychnodictyum audax</i>	2.78		
												RN11a
3	C2Ar	r	late		Opoitian (Wo)	3.2	Tau	RN10	<i>Phormostichoartus doliolum</i>	3.42		
3.5	C3n	r	early		Kapitean (Tk)	3.7	Tau	RN9	<i>Stichocorys peregrina</i>	3.87		
4	C3r	r	late		Tongaporutuan	4.6	Tau	RN8	<i>Didymocyrtis penultima</i>	4.19		
4.5	C3An	n	early		Tongaporutuan	5.2	Tau	RN7	<i>Didymocyrtis antepenultima</i>	5.6		
5	C3Ar	r	late		Tongaporutuan	5.6	Tau	RN6	<i>Dartus petterssoni</i>	6.71		
6	C3Br	r	late		Tongaporutuan	6.1	Tau	RN5	<i>Dorcadospyris alata</i>	6.71		
7	C4n	r	late		Tongaporutuan	6.6	Tau	RN4	<i>Calocyrtella costata</i>	7.7		
8	C4r	r	late		Tongaporutuan	7.7	Tau	RN3	<i>Stichocorys wolffii</i>	7.7		
9	C4An	n	early		Tongaporutuan	9.1	Tau	RN2	<i>Stichocorys delmontensis</i>	8.77		
10	C4Ar	r	late		Tongaporutuan	10.1	Tau					
11	C5n	r	late		Tongaporutuan	10.4	Tau					
12	C5r	r	late		Tongaporutuan	11.3	Tau					
13	C5An	n	early		Tongaporutuan	11.95	Tau					
14	C5Ar	r	late		Tongaporutuan	12.6	Tau					
15	C5AAn	n	early		Tongaporutuan	13.0	Tau					
16	C5AAn	n	early		Tongaporutuan	13.6	Tau					
17	C5AAn	n	early		Tongaporutuan	14.2	Tau					
18	C5ADn	r	late		Tongaporutuan	15.1	Tau					
19	C5ADr	r	late		Tongaporutuan	16.3	Tau					
19	C5Bn	r	late		Tongaporutuan	16.7	Tau					
19	C5Br	r	late		Tongaporutuan	17.0	Tau					
19	C5Cn	n	early		Tongaporutuan	17.03	Tau					
19	C5Cr	r	late		Tongaporutuan	17.92	Tau					
19	C5Dn	r	late		Tongaporutuan	19.1	Tau					
19	C5Dr	r	late		Tongaporutuan	19.4	Tau					
19	C5En	n	early		Tongaporutuan	19.4	Tau					
19	C5Er	r	late		Tongaporutuan	19.4	Tau					
19	C6n	r	late		Tongaporutuan	19.4	Tau					

Figure F9 (continued).

Age (Ma)	Chronos	Polarity	Epoch	Series	New Zealand		Takemura (1992) Abelmann (1992), Hollis (1997) South Pacific radiolarian zone		Inter-national	Sanfilippo and Nigrini (1998)						
					Stage	Ma	Code #	Tropical radiolarian zone		Ma						
19	C5Dr C5En C5Er		Miocene	Pareora	middle Altonian (Pl)	19.4	<i>Cycladophora gollii regipileus</i>	Burdigalian	RN2	<i>Stichocorys delmontensis</i>						
20	C6N C6r	early			early	early	20.2				<i>Cyrtocapsella longithorax</i>			20.53		
21	C6An C6Ar C6AAr				late	Landon	Otaian (Po)	22.4 22.5	<i>Cycladophora antiqua</i>	Aquitainian	RN1	<i>Cyrtocapsella tetrapera</i>				
22	C6AAr C6Bn C6Br						Waitakian (Lw)	25.0	<i>Lychnocanoma conica</i>				Chattian	RP22	<i>Lychnocanoma elongata</i>	23.62
23	C6Bn C6Br						Duntroonian (Ld)	27.1								Rupelian
24	C6Cn C6Cr						Whaingaroan (Lwh) early	27.5								
25	C7n C7r C7An C7Ar						Oligocene	Landon	late	30.0	<i>Axoprunum ? irregularis</i>	Rupelian	RP20	<i>Theocyrtis tuberosa</i>		
26	C8n C8r								early	33.0						
27	C9n C9r				late	34.3			<i>Eucyrtidium spinosum</i>	Priabonian	RP19				<i>Cryptocarpium ornatum</i>	~32.8
28	C10n C10r				late	35.5										
29	C11n C11r		Eocene	Arnold	Kaiatan (Ak)	37.0				Priabonian	RP18	<i>Calocyclus bandyca</i>	~36.4			
30	C12n				Bortonian (Ab)	39.0			<i>Lithapium mitra</i>				Bartonian	RP17	<i>Cryptocarpium azyx</i>	~37.7
31	C13n C13r				middle	39.0										~38.8
32	C15n C15r				middle	42.0			<i>Eusyringium fistuligerum</i>	Bartonian	RP16	<i>Podocyrtis goetheana</i>	~39.5			
33	C16n C16r		middle	42.0												
34	C17n C17r		Eocene	Arnold	Bortonian (Ab)	39.0		Bartonian	RP15	<i>Podocyrtis chalara</i>						
35	C18n C18r				Porangan (Dp)	42.0	<i>Eusyringium lagena</i>				Lutetian	RP14	<i>Podocyrtis mitra</i>			
36	C19n C19r				middle											
37	C20n				middle											

Figure F9 (continued).

Age (Ma)	Chronos	Polarity	Epoch	Series	New Zealand		Ma		Hollis (1997)		International	Sanfilippo and Nigrini (1998)	
					Stage		South Pacific Radiolarian Zones		Code #	Tropical radiolarian zone		Ma	
42	C18r C19n		Eocene	Arnold	Bortonian (Ab)	42.0	RP12	<i>Eusyringium fistuligerum</i>	Bartonian	RP14	<i>Podocyrtis mitra</i>	~42.8	
43	C20n	Porangan											44.5
44	C20r				Heretangan	46.2	RP12	<i>Thyrsocyrtis triacantha</i>					
45	C21n	(Dh)											47.0
46	C21r				Mangaorapan	49.5	RP10	<i>Cycladophora ? auriculaleporis</i>					
47	C22n	(Dm)											51.0
48	C22r				Waipawan	52.85	RP8	<i>Bekoma divaricata</i>					
49	C23n	(Dw)											53.5
50	C23r				Teurian	54.5	RP7	<i>Bekoma campechensis - Bekoma bidartensis</i>					
51	C24n	late											55.5
52	C24r		early	58.0	RP5	<i>Buryella tetratica</i>	~60.2						
53	C25n	(Dt) early						61.0	RP4	<i>Buryella foremanae</i>	Unzoned		
54	C25r		early	63.0	RP3	<i>Buryella ? granulata</i>	Unzoned						
55	C26n	early						64.0	RP2	<i>Amphisphaera kina</i>	Unzoned		
56	C26r		early	64.4	RP1	<i>Amphisphaera aotea</i>	Unzoned						
57	C27n	early						65.0	RP1	<i>Amphisphaera aotea</i>	Unzoned		
58	C27r		early	65.0	RP1	<i>Amphisphaera aotea</i>	Unzoned						
59	C28n	early						65.0	RP1	<i>Amphisphaera aotea</i>	Unzoned		
60	C28r		early	65.0	RP1	<i>Amphisphaera aotea</i>	Unzoned						
61	C29n	early						65.0	RP1	<i>Amphisphaera aotea</i>	Unzoned		
62	C29r		early	65.0	RP1	<i>Amphisphaera aotea</i>	Unzoned						
63	C29r	early						65.0	RP1	<i>Amphisphaera aotea</i>	Unzoned		

Figure F10. Comparison of the response curves for the shipboard cryogenic superconducting DC-SQUID magnetometer. These curves were obtained by passing a dipole point source through the sensor region. The half-power width of the sensors is ~ 7 cm. SQUID = superconducting quantum interference device.

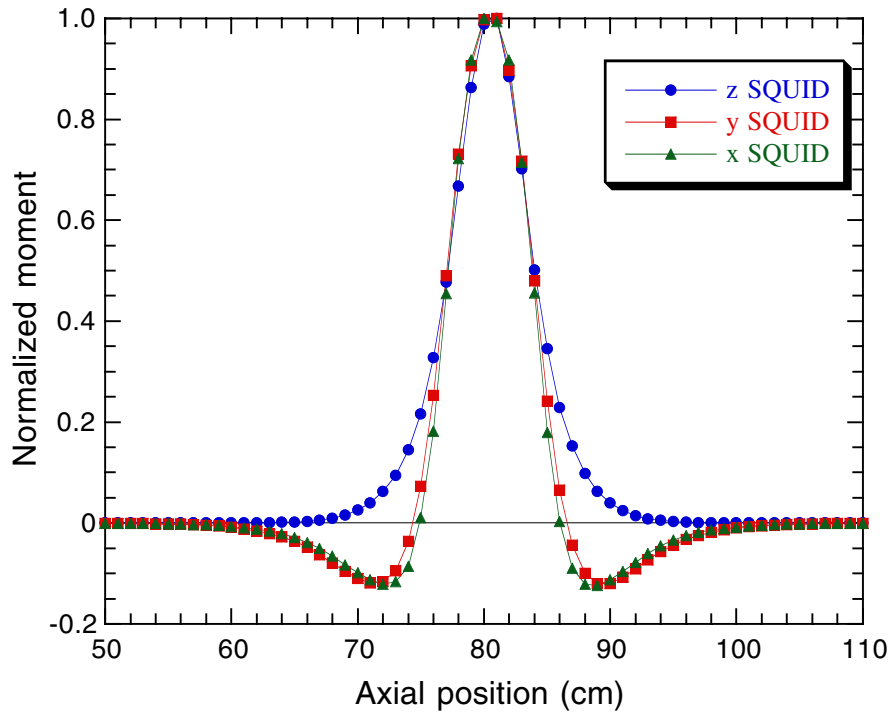


Figure F11. Total magnetic field measured inside the TSD-1 oven with a fluxgate magnetometer (model APS 520). Shaded regions = heating and cooling chambers. [N1]

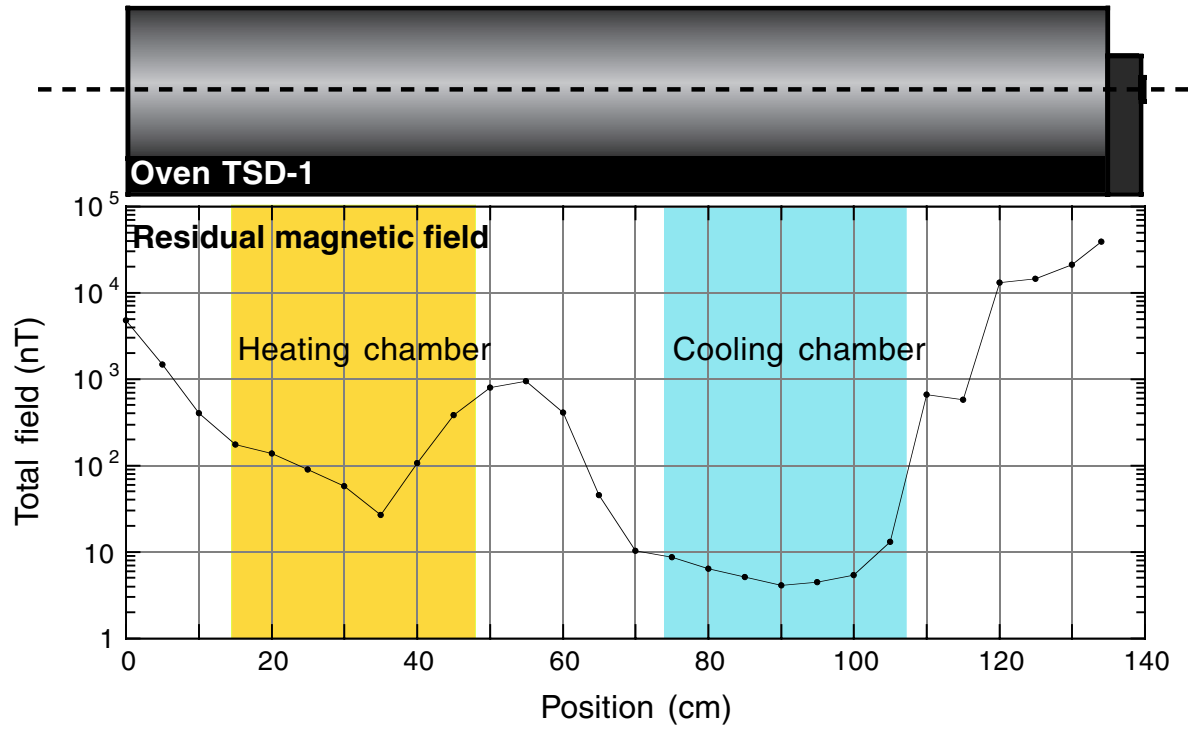


Figure F12. Core-orientation conventions for (A) split core (archive and working section) and (B) discrete cylindrical sample.

ODP core-orientation conventions

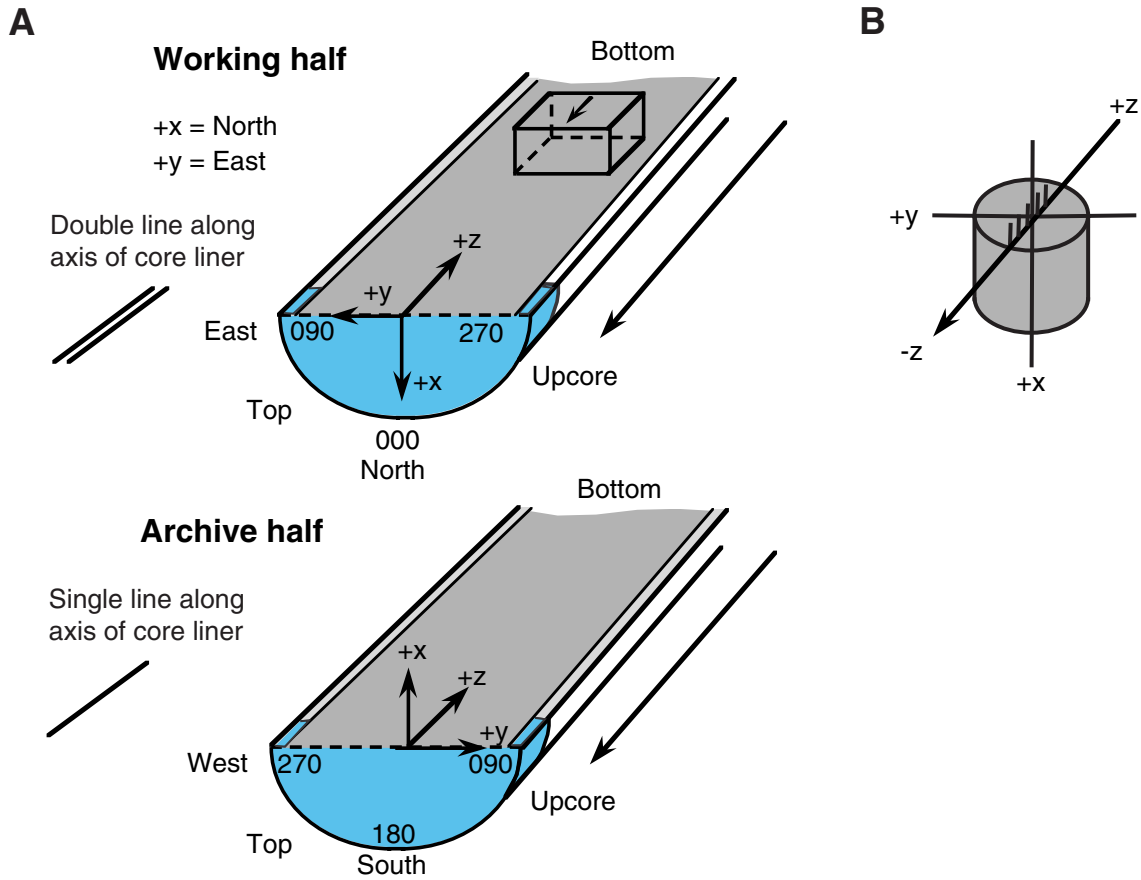


Figure F13. Response curve for the magnetic susceptibility loop on the multisensor track position as measured from the center line of the sensor. The curve was obtained from the measurement of a thin disc with a small amount of iron powder mounted in a piece of core liner. [N1]

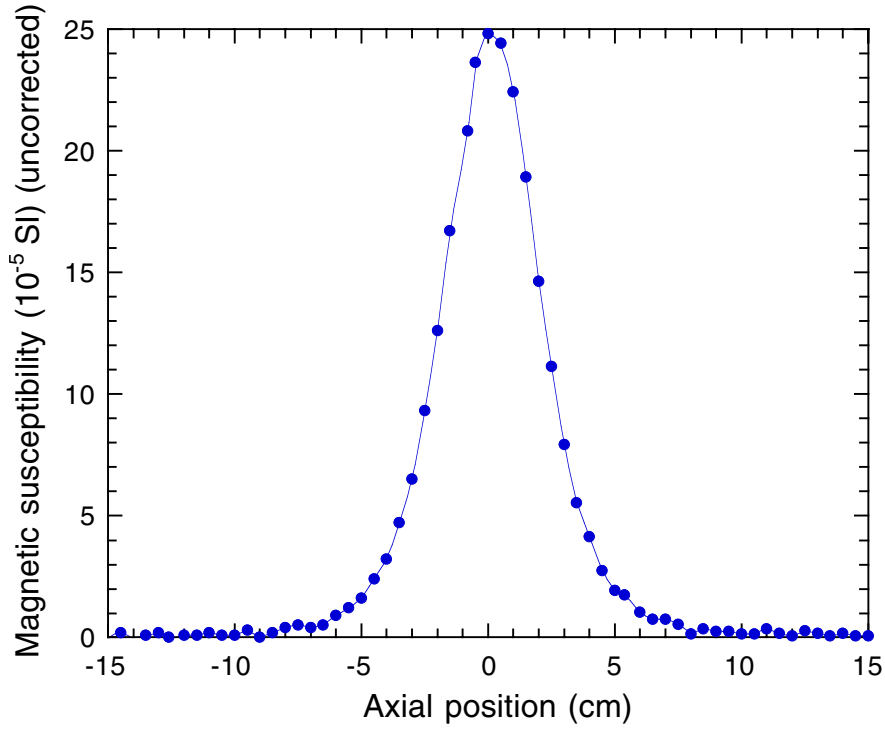


Figure F14. Wireline tool strings used during Leg 188. HNGS = hostile environment natural gamma-ray sonde, APS = accelerator porosity sonde, HLDS = hostile environment lithodensity sonde, DIT-E = dual-induction tool, NGT = natural gamma-ray tool, GPIT = general-purpose inclinometer tool, SUMS = susceptibility measurement sonde, NMRS = nuclear resonance magnetic sonde, GHMT = geological high-resolution magnetic tool, FMS = Formation MicroScanner, and DSI = dipole shear imager. The FMS/GPIT/NGT combination was run at Site 1166 (not shown).

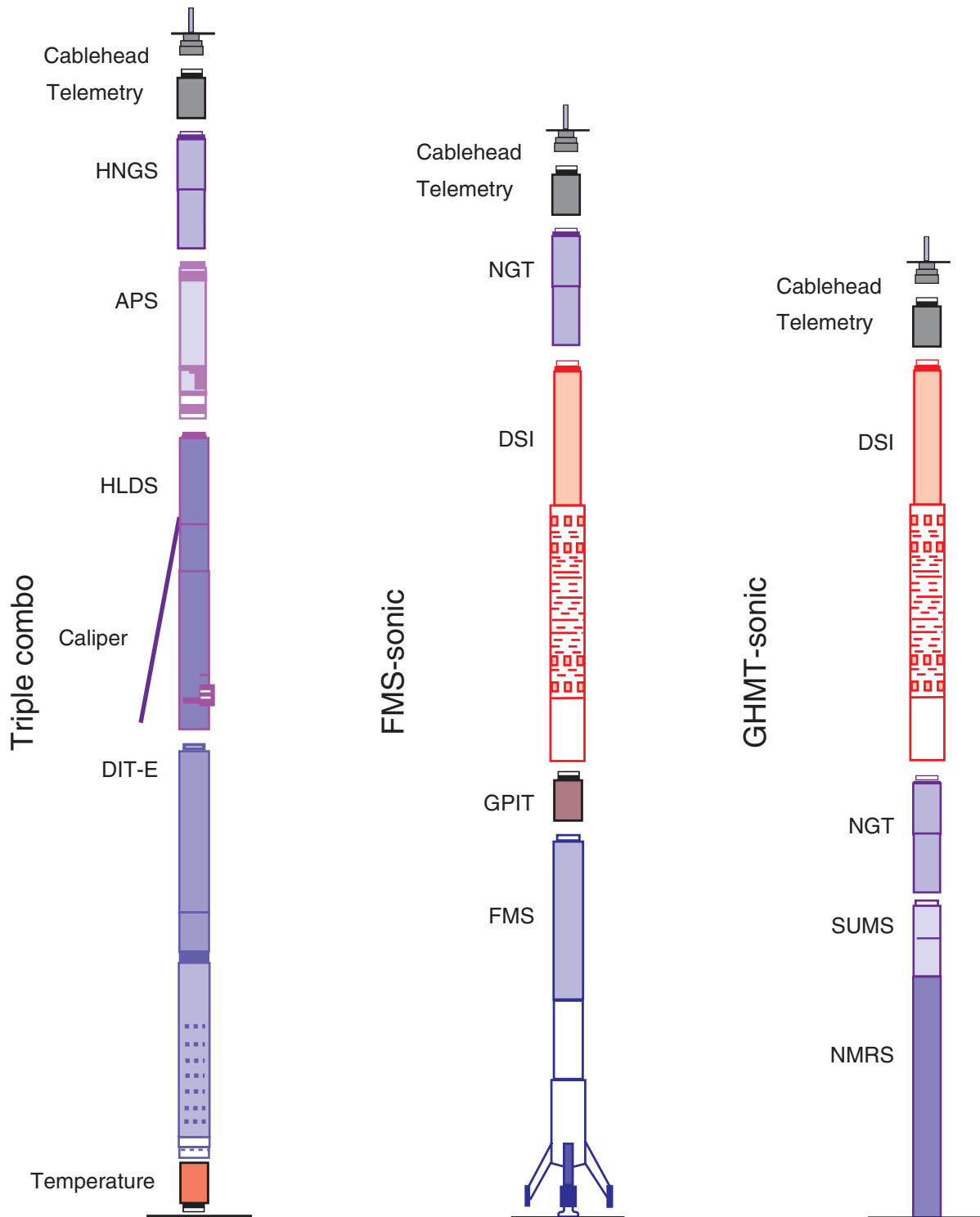


Figure F15. Schematic diagram showing the configuration of the LWD BHA. FMS-sonic was run with and without the DSI section. MWD = measurement while drilling and CDR = compensated dual resistivity tool. (Figure shown on next page.)

Figure F15 (continued). (Caption shown on previous page.)

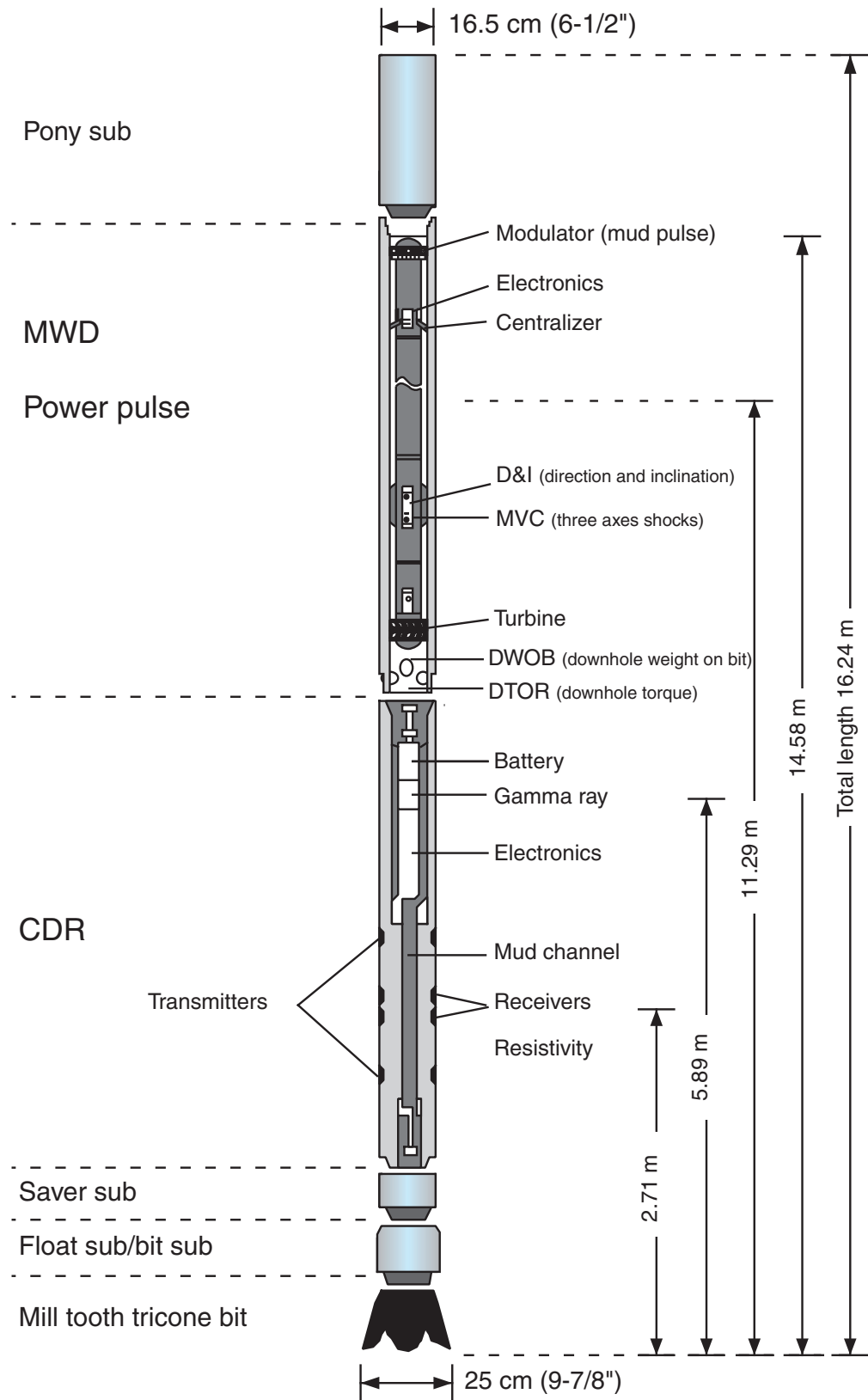


Figure F16. Schematic diagram of the FMS (adapted from Lovell et al., 1998).

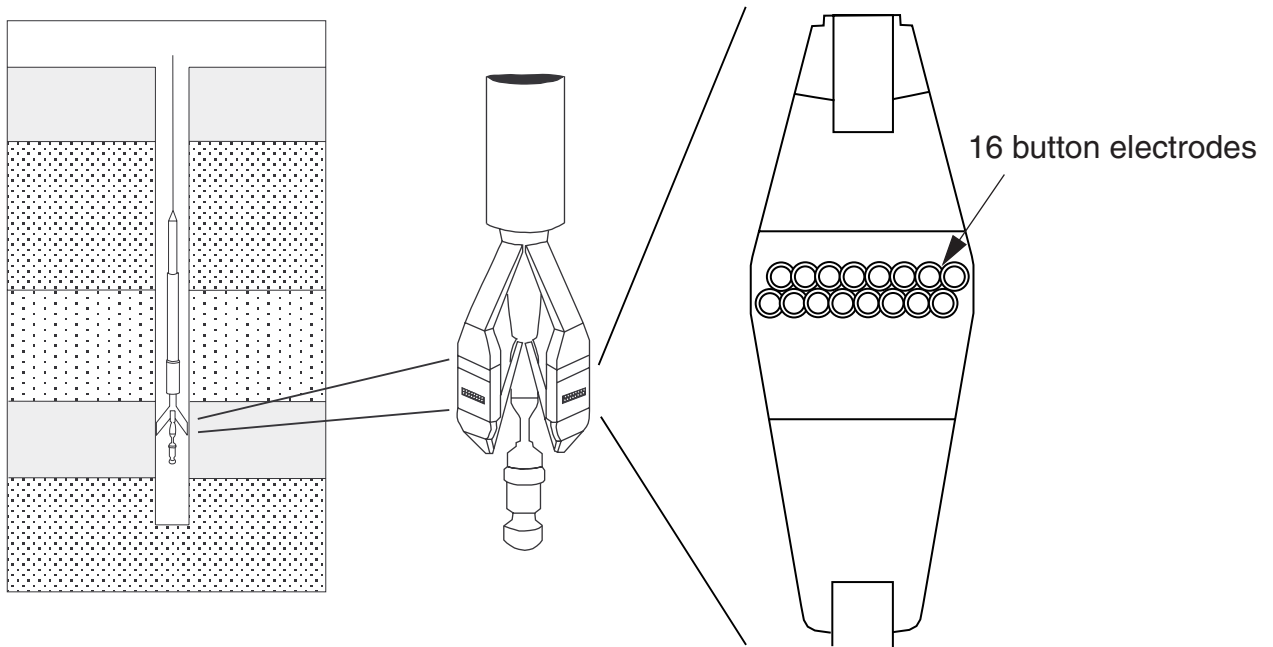


Table T1. Oligocene to Pleistocene diatom zonal ages for the Southern Ocean zonation of Harwood and Maruyama (1992).

Datum	Taxon	Revised age (Ma)
LO	<i>Actinocyclus ingens</i>	0.66
LO	<i>Fragilariopsis barronii</i>	1.35
LO	<i>Thalassiosira kolbei</i>	1.9
LO	<i>Thalassiosira vulnifica</i>	2.3
LO	<i>Thalassiosira insigna</i>	2.6
LO	<i>Fragilariopsis weaveri</i>	2.8
FO	<i>Thalassiosira vulnifica</i>	3.2
FO	<i>Fragilariopsis interfrigidaria</i>	3.8
LO	<i>Rhizosolenia costata</i>	4.2
FO	<i>Fragilariopsis barronii</i>	4.6
FCO	<i>Thalassiosira inura</i>	4.9
FO	<i>Thalassiosira oestrupii</i>	5.6-5.8
FO	<i>Thalassiosira oliverana</i>	6.4
FO	<i>Hemidiscus ovalis</i>	8.7
FO	<i>Thalassiosira torokina</i>	9.0
FO	<i>Asteromphalus kennettii</i>	10.3
LCO	<i>Denticulopsis dimorpha</i>	10.7
LO	<i>Nitzschia denticuloides</i>	11.7
FO	<i>Denticulopsis dimorpha</i>	12.2
FO	<i>Denticulopsis praedimorpha</i>	12.8
FO	<i>Nitzschia denticuloides</i>	13.5
FO	<i>Denticulopsis simonsenii</i>	14.2
FO	<i>Actinocyclus ingens</i> var. <i>nodus</i>	14.5
FO	<i>Nitzschia grossepunctata</i>	15.4
FCO	<i>Actinocyclus ingens</i>	16.2
FO	<i>"Denticulopsis" maccollumii</i>	16.7
FO	<i>Crucidenticula kanayae</i>	17.7
LO	<i>Thalassiosira praefraga</i>	18.3
LO	<i>Rossiella symmetrica</i>	19.4
FO	<i>Thalassiosira praefraga</i>	20.8
LO	<i>Azpeitia gombosi</i>	21.1
FO	<i>Thalassiosira spumellaroides</i>	22.6
LO	<i>Lisitzinia ornata</i>	24.3
LO	<i>Rocella vigilans</i> var. B	25.4
FO	<i>Rocella gelida</i>	26.4
FO	<i>Lisitzinia ornata</i>	28.0
FO	<i>Azpeitia gombosi</i>	28.3
LO	<i>Rocella vigilans</i> var. A	28.9
FO	<i>Rocella vigilans</i> var. A	30.2
FO	<i>Cavitatus jouseanus</i>	30.6
FO	<i>Rhizosolenia oligocaenica</i>	33.2

Notes: All ages are revised to the Berggren et al. (1995b) time scale. LO = last occurrence, FO = first occurrence, FCO = first common occurrence, LCO = last common occurrence.

Table T2. Ages of biostratigraphically useful radiolarian datums calibrated to the Berggren et al. (1995b) geomagnetic polarity time scale.

Age (Ma)	Radiolarian event	Source
0.18	FO <i>Buccinosphaera invaginata</i>	Johnson et al., 1989
0.46	LO <i>Stylatractus universus</i>	Caulet, 1991
0.83	LO <i>Pterocanium trilobum</i>	Lazarus, 1992
1.81	Pliocene/Pleistocene boundary	
1.92	LO <i>Eucyrtidium calvertense</i>	Lazarus, 1992
1.93	FO <i>Lithelius nautiloides</i>	Caulet, 1991
1.93	FO <i>Triceraspyris antarctica</i>	Caulet, 1991
2.42	LO <i>Helotholus vema</i>	Lazarus, 1992
2.44	LO <i>Desmospyris spongiosa</i>	Lazarus, 1992
2.61	FO <i>Cycladophora davisiana</i>	Lazarus, 1992
3.5	LO <i>Prunopyle titan</i>	Lazarus, 1992
4.57	FO <i>Helotholus vema</i>	Lazarus, 1992
4.98-5.01	FO <i>Desmospyris spongiosa</i>	Caulet, 1991
5.01-5.11	FO <i>Prunopyle titan</i>	Caulet, 1991
5.03	LCO <i>Lychnocanoma grande</i>	Lazarus, 1992
5.2	Miocene/Pliocene boundary	
6.1	LO <i>Amphymenium challengerae</i>	Lazarus, 1992
6.58	FO <i>Amphymenium challengerae</i>	Lazarus, 1992
6.79	FO <i>Lamprocyrtis heteroporos</i>	Morely and Nigrini, 1995
7.71	FO <i>Acrosphaera? labrata</i>	Lazarus, 1992
9.12	LO <i>Cycladophora spongothorax</i>	Lazarus, 1992
9.22	FCO <i>Stichocorys peregrina</i>	Lazarus, 1992
9.32	LCO <i>Ceratocyrtis stigi</i>	Lazarus, 1992
9.83	FCO <i>Ceratocyrtis stigi</i>	Lazarus, 1992
10.36	FO <i>Acrosphaera australis</i>	Lazarus, 1992
10.53	LO <i>Cycladophora humerus</i>	Lazarus, 1992
10.61	FO <i>Eucyrtidium pseudoinflatum</i>	Lazarus, 1992
10.77	LO <i>Actinomma golownini</i>	Lazarus, 1992
12.55	FO <i>Cycladophora spongothorax</i>	Lazarus, 1992
12.68	FO <i>Dendrospyris megaloccephalis</i>	Lazarus, 1992
13.61	FO <i>Actinomma golownini</i>	Lazarus, 1992
14.18	FO <i>Cycladophora humerus</i>	Lazarus, 1992
17.02	FO <i>Eucyrtidium punctatum</i>	Lazarus, 1992
19.11	FO <i>Cycladophora golli regipileus</i>	Lazarus, 1992
20.72	FO <i>Cyrtocapsella longithorax</i>	Lazarus, 1992
22.48	FO <i>Cyrtocapsella tetrapera</i>	Harwood et al., 1992
23.35-24.73	LO <i>Lithomelissa sphaerocephalis</i>	Takemura and Ling, 1997
23.8	Oligocene/Miocene boundary	
23.94-25.26	FO <i>Cycladophora campanula</i>	Caulet, 1991
23.94-25.26	FO <i>Gondwanaria hister</i>	Caulet, 1991
24.12-?28.75	LO <i>Axoprunum irregularis</i>	Takemura and Ling, 1997
26.77-30.05	LO <i>Eucyrtidium antiquum</i>	Caulet, 1991
26.77-30.05	LO <i>Lophocyrtis longiventer</i>	Caulet, 1991
?28.28-29.40	FO <i>Calocyclus</i> sp. A	Takemura and Ling, 1997
?28.28-29.40	LO <i>Lithomelissa challengerae</i>	Takemura and Ling, 1997
28.75-30.10	LO <i>Lychnocanoma conica</i>	Takemura and Ling, 1997
30.48-?33.06	LO <i>Calocyclus</i> cf. <i>semipolita</i>	Takemura and Ling, 1997
30.94-34.66	FO <i>Axoprunum irregularis</i>	Takemura and Ling, 1997
30.94-34.66	FO <i>Eucyrtidium antiquum</i>	Takemura and Ling, 1997
30.94-34.66	LO <i>Eucyrtidium spinosum</i>	Takemura and Ling, 1997

Note: FO = first occurrence, LO = last occurrence, LCO = last common occurrence, FCO = first common occurrence (Shipboard Scientific Party, 1999b).

Table T3. The wireline tool strings used and the properties measured, Leg 188.

Tool strings*	Typical logging speed (m/hr)	Individual tools*	Properties measured	Sample interval (cm)	Approximate vertical resolution (cm)	Approximate depth of investigation (cm)
Triple combo (total length ~32 m)	250-275	HNGS	Natural gamma ray	15	45	25
		APS	Porosity	5 and 15	30	15
		HLDS	Bulk density, PEF	15	38	15
		DITE-SFL	Resistivity	15	150/90/60	150/76/38
		TAP	Temperature	1 per second		
		TAP	Acceleration	4 per second		
		TAP	Pressure	1 per second		
FMS-sonic (total length ~30 m)	250-275	NGT	Natural gamma ray	15	45	45
		GPIT	Tool orientation	1 or 15		
		DSI	Sonic velocity	15	110	15-30
		FMS	Resistivity image	0.25	0.5	15
GHMT (total length ~9 m)	300-400	NGT	Natural gamma ray	15	45	25
		SUMS	Susceptibility	5 and 15	35	
		NMRS	Total field	5 and 15	45	

Notes: * = see Table T5, p. 66, for definitions of acronyms used to describe tool strings and individual tool names. PEF = photoelectric effect.

Table T4. Definitions of acronyms used to describe LWD and MWD tools.

Tool	Output	Definition	Unit
CDR		Compensated dual resistivity	
	ATR	Attenuation resistivity (deep)	Ωm
	PSR	Phase shift resistivity (shallow)	Ωm
	GR	Total gamma ray	gAPI
	SGR	Total spectral gamma ray	gAPI
	CGR	Corrected spectral gamma ray (K+Th)	gAPI
	THOR	Thorium (Th)	ppm
	URAN	Uranium (U)	ppm
	POTA	Potassium (K)	%

Table T5. Definitions of acronyms used to describe wireline tool strings and individual tool names.

Tool	Output	Definition	Unit
HNCS		Hostile environment natural gamma-ray sonde	
	HSGR	Standard (total) gamma ray	gAPI
	HCGR	Computed gamma ray (HSGR – uranium contribution)	gAPI
	HFK	Formation potassium	%
	HTHO	Thorium	ppm
	HURA	Uranium	ppm
NGT		Natural gamma-ray tool	
	SGR	Standard total gamma ray	gAPI
	CGR	Computed gamma ray (SGR – uranium contribution)	gAPI
	POTA	Potassium	%
	THOR	Thorium	ppm
	URAN	Uranium	ppm
APS		Accelerator porosity sonde	
	APLC	Near array porosity (limestone corrected)	Fraction
	FPLC	Far array porosity (limestone corrected)	Fraction
	SIGF	Neutron capture cross section of the formation (Σ_p)	capture units
	STOF	Tool standoff (computed distance from borehole wall)	In
HLDS		Hostile environment lithodensity sonde	
	RHOM	Bulk density (corrected)	g/cm ³
	PEFL	Photoelectric effect	barn/e ⁻
	LCAL	Caliper—measure of borehole diameter	In
	DRH	Bulk density correction	g/cm ³
DIT		Phasor dual-induction/spherically focused tool	
SFR		Spherically focused resistivity	
	IDPH	Deep induction phasor-processed resistivity	Ω m
	IMPH	Medium induction phasor-processed resistivity	Ω m
	SFLU	Spherically focused resistivity	Ω m
GHMT		Geologic high-sensitivity magnetic tool	
	MAGS	Magnetic susceptibility (limited range)	ppm
	RMGS	Low-resolution magnetic susceptibility (wider range)	ppm
	MAGC	Conductivity	ppm
	MAGB	Total magnetic field	nT
DSI		Dipole shear sonic imager	
	DTCO	Compressional wave transit time	μ s/ft
	DTSM	Shear wave transit time	μ s/ft
TAP		High-resolution temperature/acceleration/pressure tool	$^{\circ}$ C, m/s ² , psi
GPIT		General purpose inclinometer cartridge	
	Fx, Fy, Fz	Magnetic field (three orthogonal directions)	nT
	Ax, Ay, Az	Acceleration (three orthogonal directions)	m/s ²

CHAPTER NOTE

- N1. 5 June 2001—Erratum: The captions and images to Figures F11 and F13 were originally reversed. This version contains the correct figures.